Design and Implementation of a Novel Stationary Electromagnetic Eddy Current Separator

by

Mohammad Shahabbasi

A thesis submitted in partial fulfillment of the requirements for the degree of

Master of Science

in

Energy Systems

Department of Electrical and Computer Engineering
University of Alberta

Abstract

Metal recycling is a sustainable development which reduces greenhouse gases, maximizes the use of finite natural resources, and diverts material from landfills. Recycling can reduce the air pollution by 86%, water pollution by 76%, and energy consumption by 74%. The most common recyclable metals are aluminum and steel. The steel (Ferrous metals) can be easily separated out magnetically. Non-Ferrous metal such as Aluminum, whose productions are also very energy demanding, require more complicated sorting technologies like Eddy Current separators to recover the metal fractions. In this research, innovative magnetic structure suitable for power electronics is designed, optimized and implemented to eliminate the barriers of conventional rotating magnetic drum such as maintenance and energy consumption. Conventionally, magnetic drums are used for the separation of the non-ferrous metal. The conventional dynamic separators utilize power consuming rotors with high number of special rare earth magnetic poles, which makes them heavy, expensive and inflexible without the capability to adjust the frequency suitable for various particle sizes. Apart from dynamic separators, a number of static or stationary separators have also been proposed. However, the existing static solutions are not able to provide comparable magnetic fields to the dynamic separators and cannot achieve the required performance with an acceptable efficiency.

In this dissertation, a variety of possible magnetic structures are analyzed, simulated by FEM, designed, and modeled leading to a novel static highly flexible planar structure to eliminate the barriers of the conventional static eddy current separators. The optimum structure and magnetic field is achieved using analytical derivation of a

cost function based on practical industrial constraints. The optimized design is used to implement a scaled down prototype and the accuracy of the analytical model and FEM calculated magnetic field results are validated by experimental setup.

Acknowledgements

Table of Contents

List of Tables

List of Figures

Chapter 1

Introduction

Based on evidence in Pompeii, the history of hand recovery of metals is going back to Roman empires. Before using magnets to recover ferrous metals, separation was done manually until $1960s$ when mechanical techniques replaced human labors. It is very well known that recycling is a sustainable process which saves significant amount of energy. The energy required to produce 1kg of Steel, from iron, is about $5.55 - 13.9kWh$, Aluminum, from bauxite, around $227 - 342MJ$ and Copper, from sulfide ore, is around $60 - 125MJ$. Metal recycling significantly reduces energy consumption and thus is a sustainable development which reduces greenhouse gases, maximizes the use of finite natural resources, and diverts material from landfills. The saved energy may vary from 74% for Steel, to 85% for Copper, and up to 95% for Aluminum depending on the metal [1].

Currently, about 45% of the world annual production of steel, over 40% of the world copper production, and about 33% of the world's aluminum is produced from recycled material. Recycling can reduce the air pollution by 86%, water pollution by 76%, and energy consumption by 74%. The steel recycled in Canada each year saves enough energy to power $2.7M$ households while, the overall recycling rate of steel in Canada is about 60% that is valued at roughly $\$3B$ [1].

The most common recyclable metals are aluminum and steel. Aluminum is an infinitely recyclable material with significantly reduced energy consumption in the

next rounds of production. For example, the secondary production of the Aluminum only requires 5% energy in the primary production of the Aluminum metal from bauxite [2]. It takes only 6 weeks to recycle, re-manufacture and refill an Aluminum bottle, yet it takes 300 years for the Aluminum to be disintegrated in the landfill [3].

Normally, a scrap metal shredder is used to make smaller pieces to be sorted and separated. The steel, or generally Ferrous metals, can be easily separated out magnetically. Principles of the magnetic separations is covered by Oberteuffer in previous studies [4]. Non-Ferrous metals such as Aluminum, whose productions are also very energy demanding, require more complicated sorting technologies, such as eddy current and electrostatic separation to recover the metal fractions. This thesis is focused on eddy current separator technologies and intends to develop new more efficient and cost effective approach to implement separators.

1.1 Eddy Current Application in Separators

Based on laws of electromagnetism, it was known for years that, Lorentz force will be applied to a non-ferrous metal in a time-varying magnetic field. Accordingly, scientists tried for decades to develop a method for separating non-ferrous metals with a moving magnetic field.

The idea of producing time-varying magnetic field for separating non-ferrous metals was first introduced by Thomas Edison and Hiram Maxim back in 1889 [5], [6]. Their approach was based on the utilization of rotating electromagnets energized by dc current to produce the magnetic field . In the same year, Moffat patented an idea for a magnetic separator using a stationary structure energized by ac current to produce the required time-varying magnetic field instead of rotating electromagnet [7]. Apart from the difference in all mentioned approaches, working principle of all three patents were based on producing a time-varying magnetic field to induce eddy current on the non-ferrous metal particles. Before reviewing the development of dynamic and static eddy current separators, the theory of inducing eddy current on the non-ferrous metal

surface in a time-varying magnetic field and applied Lorentz force is discussed briefly.

1.1.1 Theory

The mechanism of eddy current separation is based on exposing conductive, non-ferrous metal particles to a time-varying magnetic field which induces an eddy current on the surface of the particles volume. Interaction of the original magnetic field and the induced current, creates a force, called Lorentz force on the metal particles. The induced force will throw away the non-ferrous conductive metals. Based on Faraday's law, a time varying magnetic field, $B(T)$, produced by an ac current will result in an electric field, $E(\frac{V}{m})$:

$$\begin{cases} \nabla \times E = -\dfrac{\partial B}{\partial t} & Time\ Domain \\ \\ \nabla \times E = -j\omega B & Frequency\ Domain \end{cases} \quad . \tag{1.1}$$

Based on Ohm's law, when a conductive material such as Aluminum or Copper is placed in the produced electric field, eddy current, $J(\frac{A}{m^2})$, is induced in the conductive material:

$$J = \sigma E \ . \tag{1.2}$$

The electrical conductivity of the material is $\sigma(\frac{S}{m})$ the reciprocal of electrical resistivity. It represents a material ability to conduct electric current. Based on Ampere's law, the new current will induce secondary magnetic field, called eddy magnetic field or B_e, to oppose the original magnetic field:

$$\nabla \times B_e = \mu_0 J \ , \tag{1.3}$$

where μ_0 is the permeability of the free space. Calculation of J under magnetic field, B, is complicated and both variables, J and B_e, should be solved simultaneously [8]. In addition, J depends on the metal particles geometry and material which makes the estimation even more complex. Basic estimations of J in simple geometries such as sphere or cylinder have been done in previous studies [9]. After calculating J, based

on the magnetic force law, the applied Lorentz force, $F_{avg}(N)$, to non-ferrous metal is:

$$F_{avg} = \frac{1}{2}Re\left\{\iiint J \times B^* \, dV\right\} \ .$$ (1.4)

Obtaining Lorentz force from (1.4) is complicated because of the dependency of the Lorentz force to the particle shape, conductivity, magnetic field magnitude and, profile. Based on the linear magnetic field profile, a closed form approximation of this force for a sphere with uniform conductivity is derived in previous studies [10]. It is shown that, the magnitude of applied Lorentz force will be increased and saturated by increasing the frequency [8]. Also, in smaller particles the force will be saturated at higher frequencies rather than larger particles with the same shape and metal material [11]. Eddy current is induced on the surface, thus, the applied force in a cubic particle will be more than the force in the same size spherical particle.

1.2 Conventional Eddy Current Separators

There are several patents in the $20th$ century that can be categorized into: dynamic and static eddy current separators. Both approaches are developed over the years. However, due to the simpler implementation of dynamic separators using electric motors, dynamic separators have been extensively used in industries for several years and major improvement in dynamic separators is not expected, while full potential of static separators is not investigated and will be the focus of this thesis.

1.2.1 Dynamic Eddy Current Separators

Modern dynamic eddy current separators utilize strong rare earth magnets. The different parts of scraps carrier system and a simple dynamic eddy current separator is shown in Fig. 1.1.
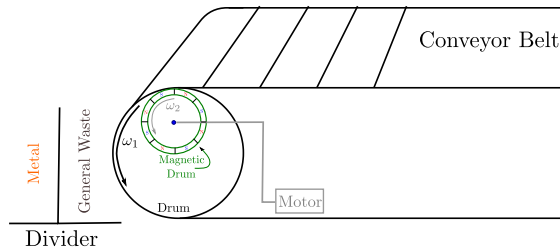
Figure 1.1: A generic structure for dynamic eddy current separators

To avoid the use of permanent magnets and to reduce costs, initially, Mccarthy, patented a dynamic separator based on the rotation of electromagnets excited by three phase current in 1922 [12]. This structure uses complex wiring, mechanical design and commutators. Almost half a decade later, Benson and Falcone patented first dynamic eddy current separator based on the rotation of permanent magnets. This structure used a simple 8 poles permanent magnet motor inside the roller drum of the waste feeder [13].

In 1988, Van der valk proposed a dynamic drum consists of two expensive rotating magnetic disks located in parallel to each other vertically [14]. The main disadvantage of Van der valk device was the challenge of increasing the operating frequency for the separation of smaller particles which was done by special mechanical infrastructure for the high speed rotation of the disks.

In 1991 Julius introduced a dynamic separator similar to Benson and Falcone approach which used a rotor placed inside the drum with 4 magnets instead of 8 [15]. One year later Roos proposed another structure with rotating permanent magnets located beneath the feeder belt instead of inside the feeder roller [16]. The disadvantage of both structures was the challenge of reaching high speed rotation and related higher losses to achieve higher frequencies [8].

Lungu et al patented several ideas for dynamic eddy current separators in the first decade of 21st century. In 2001, a vertical spinning eddy current separator

consists of 18 NdFeB magnets located at near the end of the feeder was proposed by Lungu. This structure was bulky and it occupied significant space [17]. One year later, Lungu proposed another structure with bulky rotating disks located beneath the feeder parallel to an inclined surface [18]. In 2005, Lungu proposed his last separator using a conventional rotating magnet beneath the belt surface. The contribution of the structure was to use an angular magnetic drum with rotated axis not parallel to the feeder roller axis [19]. Although, the recycling process output was promising, the structure had the challenge of achieving high frequencies and it required wider belt to fit the angular drum.

The latest dynamic separator is proposed by Yao in 2015 based on superconducting magnets [20]. Due to the presence of expensive superconducting coils, heat dissipation is the main concern in the proposed structure as it requires a special cooling system. Consequently, the implementation of the structure is not economically practical.

Nowadays, dynamic separators which are used in the industry use rotors made of strong magnet with high number of poles. One of the best industrial magnetic drums which is used in the segregation companies, is implemented by Goudsmith Inc. This separator uses 48 poles of high intensity magnets to produce around $40mT$ magnetic flux density at $3cm$ from the drum. The operating frequency of this structure is limited to $300RPM$ [21]. Because of the heavy machinery, operating beyond such low frequency is not either efficient or practical.
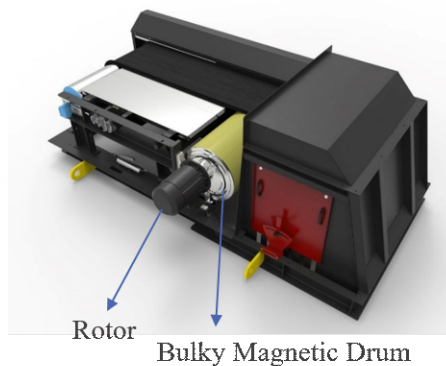
Figure 1.2: Belt and drum structure for Goudsmith Inc. eddy current separator [21]

6

1.2.2 Static Eddy Current Separators

Similar to dynamic separators, several projects have been proposed to develop a reliable and affordable static eddy current separator. Back in 1931 Royal proposed a simple coil excited with ac current to produce the moving magnetic field [22].

Another possibility to have a static separator is to move particles fast enough in the vicinity of a magnetic field. In 1975, Schlömann proposed a structure with a 45° ramp using alternating poles made from stationary permanent magnets beneath the angular ramp. In the proposed structure, movement of the scraps alongside the ramp would produce the alternating magnetic field. The main disadvantage was the dependency of the produced magnetic field frequency to the initial velocity of the particles. The velocity itself was not a controllable variable and it depended on the weight and geometry of the particles [23].

Four years later, Schlömann and Reiner introduced a static separator for $1 - 5mm$ metal scraps. The main idea, also known as channel separator, is to place permanent magnets at the side of inclined steel plates instead of beneath the ramp [24].

One year later in 1980, Zakharova proposed a electromagnet based structure with perpendicular magnetic fields. The first electromagnet intended to orient the conductive particles and the second one was to sort them out. The method was never verified by experiment and the theoretical background was not adequate either [25].

Another stationary separator, also known as Vertical Eddy Current Separator (VECS), was introduced by researchers in Delft university in 1988. The structure was used two vertical aluminum steel sheets with permanent magnets beneath them to separate non-ferrous metals. Although, the power consumption and the $O\&M$ cost of the structure was almost zero, it could not provide enough force for repelling small pieces of metal particles [14].

In 1995, Arnold and Bills used a $200 - 400Hz$ solenoid to generate variable magnetic field operating as an eddy current separator. The main drawback was the high

power consumption and accordingly the heat dissipation of the separator when the conductive particles were exposed to the working region of the structure [26]. Three years later, an ac excited torroidal structure with a gap introduced by Saviliev. This eddy current separator had the benefit of adjusting the frequency for recycling the particles in different sizes.

The most recent proposed structure of stationary eddy current separators is presented by Rajamani and et al at Utah university. The proposed device is a torroidal structure inspired by Saviliev and Moffat's idea [8]. The proposed electrodynamic sorting, EDX, structure is the first structure which reaches frequencies as high as $10kHz$. Industrial size EDX, successfully separated $5-25mm$ non-ferrous metal particles. The main drawback of EDX is the electrical efficiency of the structure, which is low due to presence of huge ferrite core with the the estimated loss of $200W$ for $600W$ input power with a $25A$ injected sinusoidal current at the frequency of $12kHZ$ [27]. The voltage across the EDX coil is approximately $4kV$ which makes it extremely dangerous for operation without special electrically isolated materials around the coil.

Although, mechanical aspect of static separators does not have the complexity of dynamic separators, an efficient, scalable and practical implementation of these separators is still a challenge that should be addressed with recent advancements in power electronics. In fact, none of the mentioned attempts have been optimized neither mechanically or electrically to perform non-ferrous metal segregation.
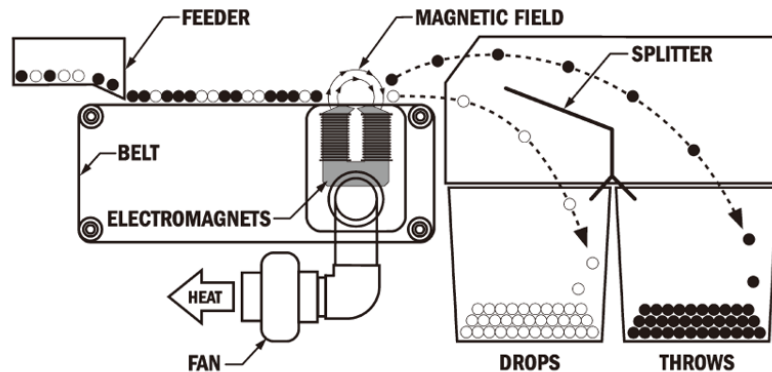
Figure 1.3: Structure of the EDX [27]

8

1.2.3 Comparison of Dynamic vs Static Separators

Dynamic separators do not have any complexity in the electrical aspect of their structure and a motor is only needed to change the magnetic field which made the dynamic separators feasible to be commercialized very soon and became popular as the design and implementation of magnetic drums is close to that of the electric machines well-practiced for decades.

Conventional magnetic drums use large electric machines with rotating magnetic drum leading to a power hungry, bulky, heavy, noisy and, expensive product as high quality strong magnets are needed in large volume to build the drum. The operation and maintenance $(O\&M)$ cost of magnetic drums are also very high due to the constant motion of the heavy structures. Despite the disadvantages of dynamic separators, utilizing strong magnets leads to high magnetic flux density at the feeder belt.

Although, the static separators generally have a simpler mechanical structure, a power electronic circuit is needed to generate strong varying magnetic field which makes static separators more complex than dynamic separators. According to recent advancements in power electronic technologies, the electrical circuit of static separators can be designed and implemented very simple, fast and most importantly in an affordable way. Although, static separators are expected to become popular again, still there is a need for an **optimized** and **efficient** static separator to compete with strong special magnets in dynamic eddy current separators.

The strong rare earth magnets in industrial dynamic eddy current separators, is a simple way to provide high magnetic flux density at the feeder belt although at a high $O\&M$. Due to the bulky structure of the dynamic separators, to achieve even $1kHz$, the separator should be rotated at $60,000RPM$ which is not practical for the huge inert structure.

On the other hand, static separators should be optimized both electrically and

mechanically to have the same magnetic flux density with a reasonable loss. Furthermore, regarding to advancements in the power electronics area, achieving high frequencies like, $100kHz$, is not a problem for static separators even though, existing industrial static separators are not optimized to operate efficiently and did not utilize power electronic circuits.

1.3 Description of Proposed Research and Thesis content

In this dissertation, a static non-planar magnetic structure for recycling non-ferrous metals is introduced. Placing a conductive particle in a magnetic field, leads to the induction of eddy current on the surface of the particle. The interaction between the magnetic field and induced eddy current, will produce a force, known as Lorentz force, on the conductive particle. The working principle of non-ferrous metal separators is based on the induced eddy current on a conductive material in the presence of a magnetic field and accordingly, the applied Lorentz force which leads to repulsion and separation of the metal particles that are normally mixed with other materials on the belt.

Based on the proposed idea, best place for the magnetic structure is in the drum of conveyor system which carries the scraps as shown in Fig.1.4. As a result, dimensions of the structure should not be greater than drum's diameter.
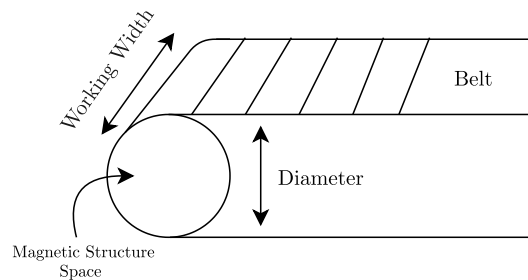
Figure 1.4: Belt and drum structure for demonstrating the usable space

In this dissertation, an innovative highly flexible power electronic circuit is proposed to eliminate the barriers of conventional approaches such as maintenance cost and frequency limited operation of dynamic separators and energy consumption, non-efficient and non-optimized operation of the static separators to recycle non-ferrous metals in an affordable and eco-friendly way.

The proposed structure and the power converter are all fitted in the drum of the feeder, accordingly all of the moving parts of the conventional magnetic rotors presented in Fig.1.1, such as the magnetic drum and the motor is replaced by a stationary structure as shown in Fig.1.5. Some of the advantages of the proposed structure over the commercial magnetic rotor based eddy current separators is presented in table 1.1.
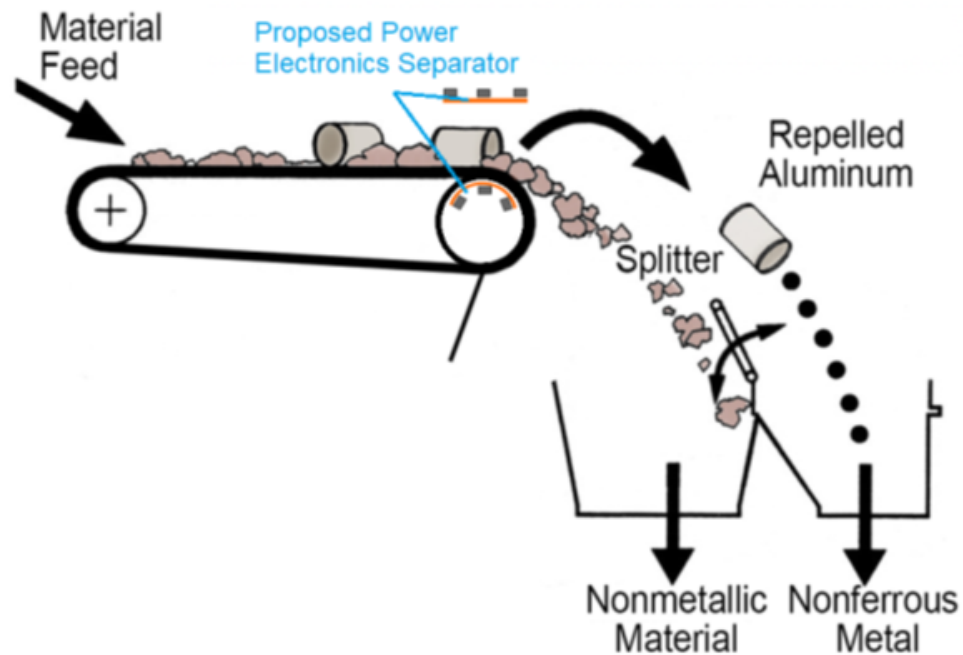
Figure 1.5: The proposed planar structure

Table 1.1: Proposed Structure Advantages

Feature	Magnetic Drum	Proposed Structure
Initial Cost	Extremely High	90% less
O&M Cost	High	Very Low
Moving Parts	Yes	No
Special Material	Strong Magnets	No
Operating Frequency	Limited	$50Hz - 250kHz$
Frequency Change	Very Slow	Instantaneous
Startup Time	High	Spontaneous
Assembly	Very Hard	DIY
Sound Pollution	Yes	No
Weight	Bulky	Light Weight
Power Electronic Based	Yes	No

To develop the stationary structure, first the most obvious structure which is simple coil without any core is analyzed. A ferrite core is added to maintain the magnetic field outside the core. Second coil is added for further improvement in the magnetic field and completing the development of the non-planar magnetic structure. All of the derived analytical models are verified by Ansys Maxwell software and drawbacks of the non-planar structure are pointed out.

To eliminate the and limitations of the non-planar structure, a novel highly flexible planar structure with less core material is introduced. The complete analytical model of the planar structure is obtained and verified by Ansys maxwell. The advantages of the proposed planar structure is pointed out by performing various FEM based test on both planar and non-planar structure.

To obtain the best performance from the proposed structure, optimized design variables of the proposed static structure is obtained from the derived optimization cost function with industrial constraints. The optimized lab scale structure is implemented

to verify the analytical and FEM based results. The overview of this dissertation is presented in Fig.1.6.
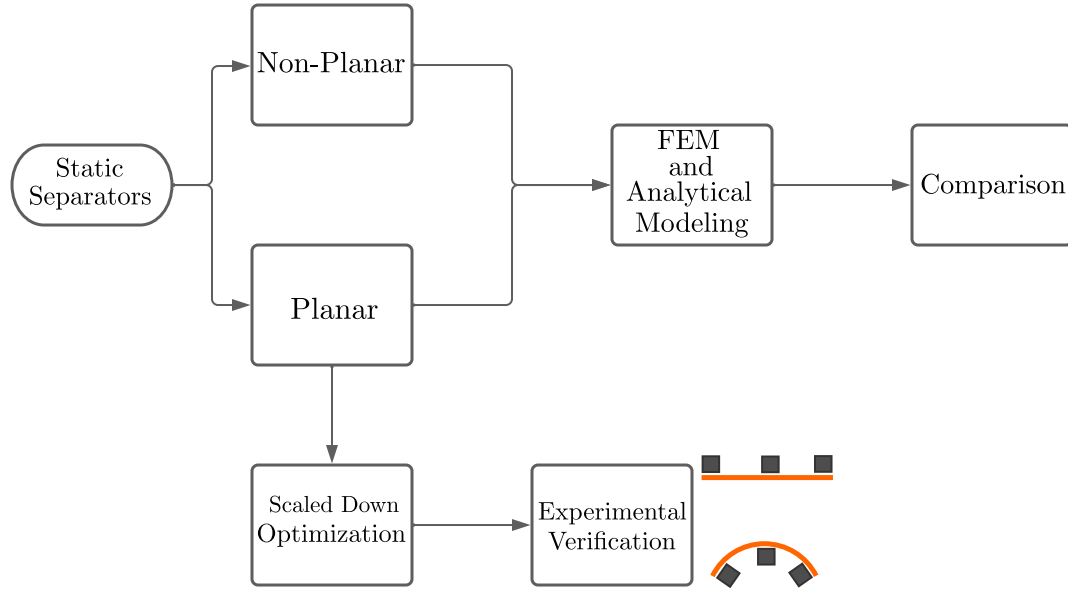
Figure 1.6: Overview of this dissertation

1.4 Thesis Objectives

The main objective of this thesis is to introduce and design an efficient and affordable static planar eddy current separator to recycle the non-ferrous metals in segregation facilities. The benefit of this structure is that, the circuit can be placed inside the conventional industrial magnetic drum without any need to change the structure of the feeder belt or roller. Briefly, this dissertation objectives can be listed as follows:

1. Obtaining the analytical and FEM model of non-planar structure.

2. Obtaining the analytical and FEM model of proposed planar structure and elaborating the advantages of flexible planar structure over the non-planar

3. Deriving the optimized planar structure which can be placed inside the pre-existing belt roller and solving the optimization problem for a lab scale structure to achieve the optimal design variables.

4. Implementing the optimized scaled down solution and obtaining the actual magnitude flux density measurements in various distances to compare it with calculated results.

Chapter 2

Non-planar Magnetic Structure Development

The proposed static separator requires a magnetic component derived by power converters to generate the variable magnetic field on the belt and to induce the eddy current in the small metal particles as explained in Fig.1.5. In this chapter the working principle of eddy current separators are discussed and it is determined how much magnetic field can be generated using the most simple magnetic structures.

A simple coil without any core is examined and using analytical model of the structure verified by FEM calculations in Ansys Maxwell software it is shown that air core structure cannot produce the required magnetic field outside the winding. It is also shown that using an E core it is possible to increase the field outside the winding. For various sizes of the E cores and using FEM calculations and analytical results, it is shown that a compact E core would not improve the magnetic flux density outside the coil enough and a large E core is required to improve the magnetic field significantly.

To further increase the magnetic field, a novel resonator coil structure is proposed to improve the magnitude of flux density between the coils at a desired distance. Based on the equivalent circuit model of two E core structure, it is shown that, magnitude and phase of the current of the second coil can be adjusted using proper design to have the maximum effect on improving the magnetic field. Similarly, FEM analysis is used

to verify the calculations and to estimate core losses. Limitations and drawbacks of non-planar structures are highlighted based on which, an alternative planar separator with concentric turns is proposed in the next chapters to improve the operation of the planar structure while reducing the total losses of the structure.

2.1   Studied Basic Non-planar Magnetic Structures

The working principle of non-ferrous metal separators is based on the Lorentz force which is caused by the interaction between the magnetic field in the space, $B(T)$, and the induced eddy current on the particles surface, $J(\frac{A}{m^2})$, which can be calculated as follows:

$$F_{avg.} = \frac{1}{2} Re \left\{ \iiint J \times B^* \, dV \right\} .$$
(2.1)

The integral in the (2.1) is over the volume of the conductive particle. Calculating Lorentz force depends on the metal's geometry, magnetic field's magnitude and profile and, the induced eddy current on the conductive material which can be done only for special cases with strict constraints [8]. Also, it is known that the magnitude of Lorentz force is increased and saturated by increasing the frequency [11]. The Induced eddy current is proportional to the particles area which is lower in smaller scraps although, due to lower mass of these particles, smaller force is needed to recycle tiny metal scraps. Consequently, to increase the magnitude of the Lorentz force, apart from the operating frequency, the only variable which can be improved by using an optimized magnetic structure is the magnetic field at the desired point in the space where the conductive materials are carried by the feeder's belt. The heat dissipation of the structure caused by both core and conduction losses should be kept as low as possible for efficient operation of the structure.

All planar and non-planar structures are compared using the same standard test conditions. The injected current is a $10A$ sinusoidal current, with the frequency of $85kHz$ which is beyond human audible range and based on WPT standardization

it is in the acceptable frequency range outside the radio frequency beam [28]. Also, this frequency is beyond the human audible spectrum that makes the structure noiseless. As shown in previous studies, further increase in the operating frequency is not beneficial as the force magnitude is saturated even for small metal particles [11].

Litz wire is used to minimize the ac conduction losses due to skin and proximity effect. Based on market availability, the best Litz wire which is suitable for $85kHz$ frequency and can withstand $10A$ current, is $1.76mm - 180 \times AWG38$ wire. The magnetic flux density at $3cm$ from the structure's surface is calculated and verified by FEM as a reference point for all of the designs. Also, the applied force to a sample $3mm$ copper sphere located at $3cm$ of each structure surface is obtained from Ansys. Although, industrial separators have at least $1m$ working length which is shown in Fig.2.1, for simplicity, in this dissertation, the working length is considered to be $2cm$ as this length would not affect the magnitude of magnetic flux density. The diameter of the imaginary drum is considered to be $3cm$ which can be filled with 15 turns from the selected Litz wire considering $0.1mm$ spacing between turns.

The E core for fitting all turns around the centre leg is Ferroxcube $E/80/38/20$ and according to the operation frequency, the selected material is $3C94$. These non-planar structures are analyzed in the following sections.
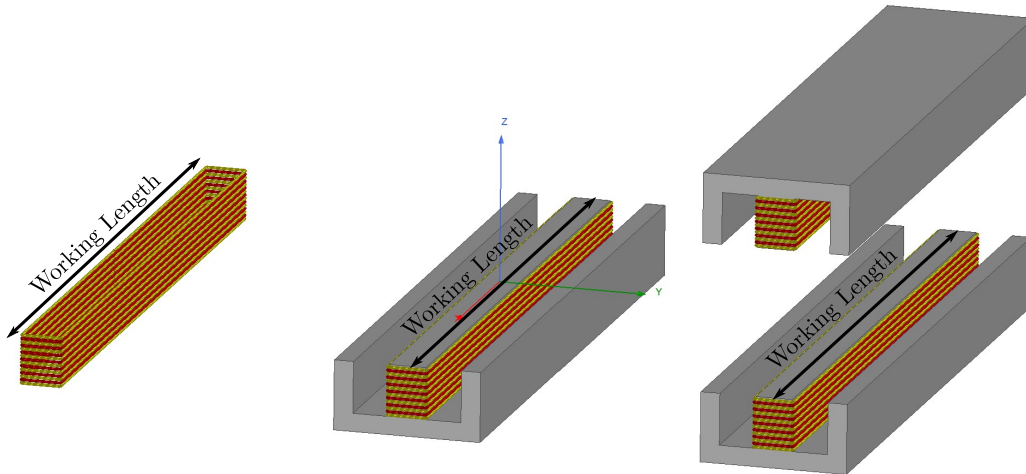
Figure 2.1: Proposed non-planar structures for Non-ferrous metals separation

2.2   Air Core Structure

The most simple design that can generate the magnetic field in the space is an air core coil which consists of square shape turns as shown in Fig. 2.2. The air core structure total loss is expected to be the lowest between all other structures as its loss is limited to conduction only. The air core structure does not provide focused flux lines uniformly distributed in the relatively high air reluctance. Consequently, this structure is expected to have the lowest magnetic flux density at the desired point, S, in Fig.2.2.

   As in the next chapters, various structures are going to be designed, and analyzed and compared, air core structures are modeled, and the magnetic flux density in the space is calculated and, then verified by FEM simulation.
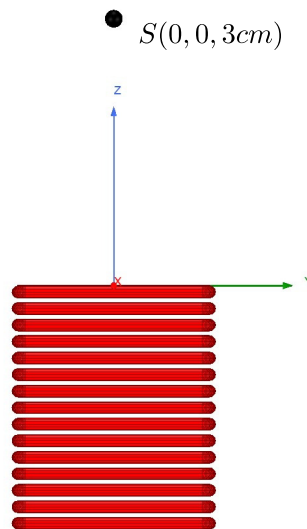
Figure 2.2: Air core structure

2.2.1   Modeling of Air Core Structure

The modeling of the air core structure starts with obtaining the magnetic flux density caused by a single and closed current carrying wire. The most fundamental law for computation of magnetic flux caused by a dc or ac current carrying wire is Biot-

Savart law. Air core structure consists 15 independent single turns, therefore, after obtaining the magnetic flux density caused by a single wire, superposition method is used to calculate the total magnetic flux density caused by the air core structure. The desired point in the space id $3cm$ from the first turn of the structure.

Biot-Savart Law

Generally, Biot-Savart law is used to obtain the magnetic flux density caused by a dc current. Although, in ac currents, if the distance between the coil and desired point in the space is much less than the wavelength of the magnetic field, Biot-Savart law can be used. The wavelength of a $85kHz$ wave is $562m$ which is much longer than the distance of the desire point to the structure which is $3cm$. Based on Biot-Savart law, magnetic flux density, B, caused by a current carrying wire in a distance, $r(m)$, can be obtained by:

$$\vec{B} = \frac{\mu_0}{4\pi} \int_v \frac{\vec{J} \times \vec{r}}{r^3} \, dv \ . \tag{2.2}$$

Current density vector is $\vec{J}$, and $\vec{r}$ is the vector between current element and desired point in the space. Uniform current density, J, in the cross sectional area of the wire, simplifies integral over the volume in (2.2) to a line integral along the wire path as follows:

$$\vec{B} = \frac{\mu_0}{4\pi} \int \frac{\vec{I} \times \vec{r}}{r^3} \, dl = \frac{\mu_0 I}{4\pi} \int \frac{\vec{dl} \times \vec{r}}{r^3} \ . \tag{2.3}$$

According to (2.3), in a rectangular shaped wire, magnetic field, B, in distance $z = d$ meter along the axis of a $l \times w$ rectangular wire as shown in Fig.2.3 is [29]:

$$\vec{B}(l, w, d) = 2\frac{\mu_0 I}{\pi} [\frac{wl}{(l^2 + 4d^2)\sqrt{l^2 + w^2 + 4d^2}} + \frac{lw}{(w^2 + 4d^2)\sqrt{w^2 + l^2 + 4d^2}}]\vec{a_z} \ . \tag{2.4}$$
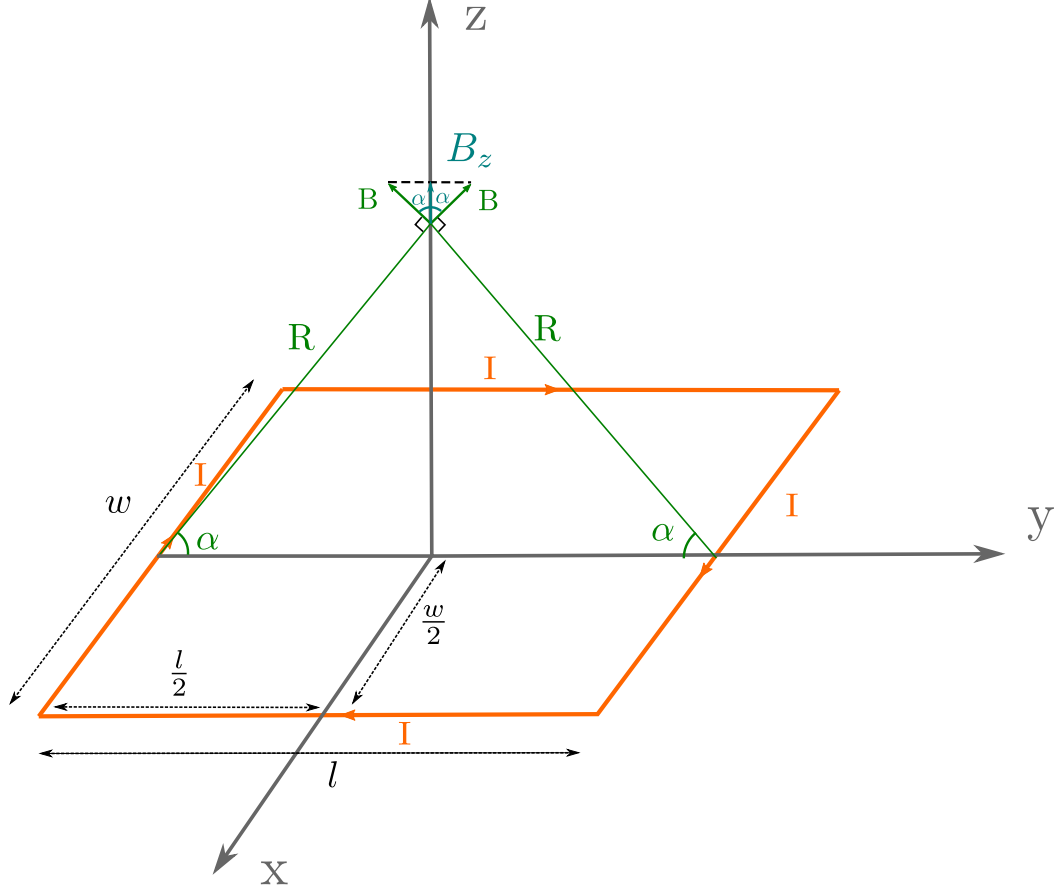
Figure 2.3: Calculating B in the axis of a square wire

Using (2.4) for a square wire, $l = w$, simplifies the equation as follows:

$$\vec{B}(l, d) = \frac{2\sqrt{2}\mu_0 I}{\pi} \frac{l^2}{(l^2 + 4d^2)\sqrt{l^2 + 2d^2}} \vec{a_z} .$$ (2.5)

The magnetic flux density along the axis of each turn in the air core structure can be calculated using (2.5). Accordingly, in the next section, based on the proposed air core structure and using the superposition method, the values of the variables in (2.5) are obtained to calculate the total magnetic flux density caused by the proposed air core structure.

Magnetic flux Density Calculation of the Air Core Structure

In this section, the objective is to calculate the magnetic flux density, B, in the distance, d, which is $3cm$ along the coil axis of the air core structure. Superposition

method is used to calculate the total magnetic field generated by the proposed air core structure. Number of turns, N, is 15 where are square shaped with the length, l, of $20mm$ with $0.1mm$ spacing between each turn. The distance from the ith turn in coil to the desired point in the space, $d_i(mm)$ can be calculated as follows:

$$d_i = d + (i - 1) \times (1.76 + 0.1)mm \ . \tag{2.6}$$

According to the superposition method, (2.5),and (3.2) the total magnetic flux density at $3cm$ from the coil is obtained as:

$$\vec{B} = \sum_{i=1}^{N} \vec{B}_i(l, d_i) = 235.3 \ \vec{a_z} \ \mu T \ . \tag{2.7}$$

The Ansys Maxwell FEM simulation is performed in the next section to obtain the complete conduction loss and verify the calculated magnetic flux density value from (2.7).

2.2.2 FEM Verification

The simulated structure in the Ansys environment is presented in Fig.2.2. Ansys Maxwell obtained magnetic flux density at $3cm$ from the coil is 232.1 μT which verifies the analytical value with 1.38% error. The applied force to the copper sphere is $186.55nN$. The obtained conduction loss from Maxwell is $2.16W$ including losses caused by proximity and skin effect. The value of magnetic field density with respect to the distance from coil along the structure's axis is presented along with the magnetic field vectors in Fig.2.4.

One can see that, air core structure cannot maintain magnetic field outside the coil and the field will drop by 94.5% from $4.5mT$ at the coil surface to 232 μT at $3cm$ of the structure. Adding a ferrite core in air core separator will provide a low reluctance path for magnetic flux to improve the focus of flux lines outside the structure. Air core winding with an E core, called E core structure, is analyzed in the next section to determine the effect of adding a ferrite core in maintaining the magnetic flux density outside the structure.
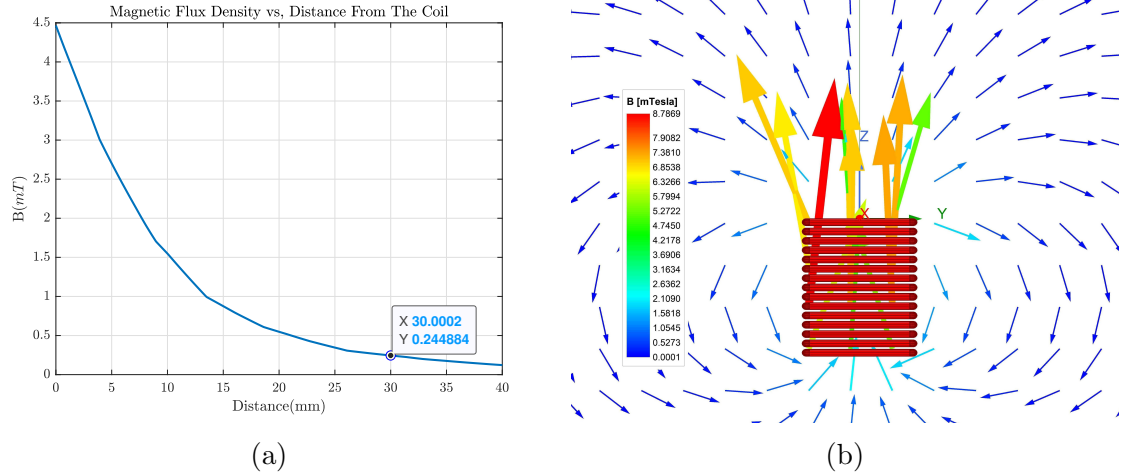
Figure 2.4: Magnetic field of air core structure (a) Magnitude with respect to distance (b) Vectors

2.3   E core

The obtained results from the previous section, determines that a simple coil cannot maintain the magnetic flux density outside the winding as the flux lines are not focused. Adding a ferrite core to air core winding will focus the flux to improve the magnetic field outside the structure. The most simple ferrite core which is E core is added to the previous structure to analyze the effect of core on focusing the flux lines.

Using core, will add core related losses to the pre-existing conduction losses. The E core structure is analyzed by defining the specifications of selected core. The mirror method is introduced to model the effect of ferrite core and based on the proposed method, the complete analytical model of the E core structure is obtained. Based on the derived model, the total magnetic flux density caused by the E core structure is calculated. The analytical model is obtained with FEM analysis.

At the end of this section, the effect of core size on maintaining the field outside the core is examined. To do so, the winding area of a compact E core, called concentrated E core, is utilized. Due to the complexity in the calculation process of multi layer winding structures with ferrite core, only FEM analysis is performed. It is shown that, compact core cannot maintain the magnetic field outside the core. Further comparison

22

between different structures is presented in the third chapter of this dissertation.

2.3.1   E Core Structure

Aiming to determine the effect of ferrite core, the $E80/38/20$ core is added to 15 turns square shape wire of the previous structure. The injected current to the structure is the same sinusoidal current with RMS value of $10A$ and frequency of $85kHz$. The mirror method in previous studies [30], is used to model the effect of core which is verified by FEM calculation from Ansys Maxwell. The Ferroxcube's E30/15/7 core [31], is selected for the compact E core structure which can be filled completely by 15 turns from the selected Litz wire. Based on availability and operating frequency of $85kHz$, the best core material to be used in both structures is Ferroxcube's $3C94$ [32]. The analytical modeling of the E core is needed prior to obtain the magnetic field.

2.3.2   Modeling of E Core Structure

The E core structure includes 15 turns of $1.76mm - 180 \times AWG38$ wire on the center leg of the $E80/38/20$ core as shown in Fig.2.5.
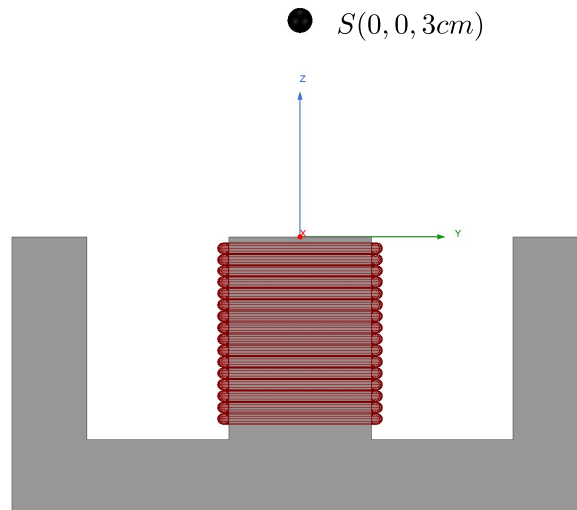
Figure 2.5: E 80/38/20 3C94 core structure

The derived model based on Biot-Savart law in the previous section, is only valid in the homogeneous environment. Hence, the model cannot be used when core exists in the structure. The effect of core should be modeled using magnetic mirroring method before using the Biot-Savart law. This method is introduced in [30] and used in several studies such as [33] and [34]. The detailed explanation of this method is presented in the next part.

Mirror method

The concept of magnetic mirroring is similar to electrical mirroring. Based on this method, the effect of an infinite magnetic plane can be calculated by replacing the plane with the image of the original current with respect to the surface of the magnetic plane to satisfy the boundary conditions. Based on electromagnetic boundary condition, there should be zero magnetic field on the coordinates of the magnetic plan surface. Therefore, the value of the imaginary current is:

$$I_{image} = \frac{\mu - 1}{\mu + 1} I_{winding} = k I_{winding} \ . \tag{2.8}$$

In materials with high relative permeability, as k reaches to 1, the current in the image conductor is the same as the actual coil. The direction of the mirror current based on the orientation of actual current with respect to the plane magnetic surface is shown Fig.2.6.
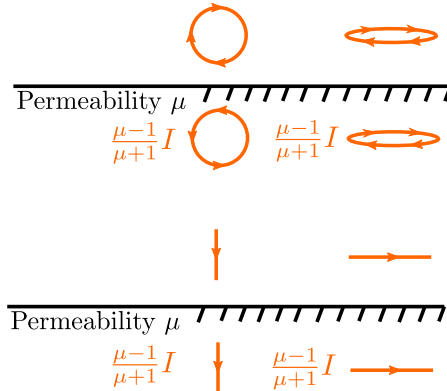
Figure 2.6: Images of current in a plane magnetic surface

In Magnetic surfaces with finite thickness, w, if the conductor is placed at $(0,0,0)$ and the magnetic material with constant permeability is located at $(0,0,z_i)$, except from the first image current in (2.8) located at $(0,0,2z_i)$, there are infinite set of image currents [35]. The nth current is at $(0,0,2z_i + 2(n-1)w)$ with the magnitude of:

$$I_{image_n} = -k^{n-1}(1-k^n)I_{winding} \qquad for\ n \geq 2 \ . \tag{2.9}$$

One can see for a finite magnetic material, thickness related image currents are in the opposite direction with respect to the actual and first image current and decreasing by a factor of k^2. Again, in materials with high permeability, the effect of core thickness can be neglected as $(1-k^2)$ reaches to zero [36].

When the winding is placed in the window of a single ferrite core which is the case for second structure, as shown in Fig. 2.7, each side of the core acts like a mirror. Consequently, similar to optics, when two parallel mirrors yield an infinite set of images, infinite number of image currents is needed to reproduce boundaries of the magnetic core [37]. Because of high permeability of ferrite materials like the $3C94$, the core thickness can be neglected for the proposed structure.

Figure 2.7: Incomplete inside window (IW) winding (a) Side View (b) Top View

Two layers of image currents produced by all three boundaries of an single E core is presented in Fig.2.8. In the mth layer of an incomplete inside window, or IW winding, there are $4m+1$ image currents. Generally, considering 2 or 3 image layers, and not infinite layers, is adequate to reproduce the core boundaries with an acceptable error. The mirror method is used in the next section to predict the effect of ferrite core and to calculate the magnetic flux density at a desired distance.
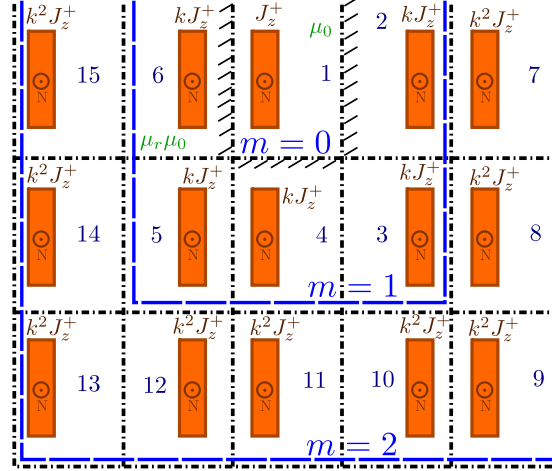
Figure 2.8: two layer images of an incomplete IW winding

Magnetic flux Density Calculation of E Core Structure

After replacing the core with image currents, superposition method is used for computing the magnetic field on the axis of the structure and in the desired distance which is $3cm$ from the structure's surface. Wire diameter is $1.76mm$ with $0.1mm$ spacing between the turns. Two layers of image current is considered for reproducing the boundaries of the core. Due to 14 image currents, computation effort for the second structure is 15 times slower than the air core in section 2.2.

One can see in Fig.2.7b that, only side parts of each turn are between two core surfaces and accordingly will have infinite set of images. Consequently, as top and bottom part of the turns are not between two core surfaces there is only one image current for the upper and lower parts.

Due to the presence of incomplete turns in image currents, only first term of (2.4) is used in the calculations which represents the magnetic flux density caused by side parts of each turn. Turn's length, l, is equal to $20mm$ which is the actual winding's length but the distance between side part of the turns which is w in (2.4) for image currents is different. In two layers of image currents, there are four different width values. Considering the fact that in E80/38/20 the window area width is $19.6mm$ the

different width values are:

$$\begin{cases} w_o = l, & o \in \{1,4,11\} \\ w_o = l + 2 \times 1.86, & o \in \{5,6,12\} \\ w_o = l + 2 \times 19.6, & o \in \{7,8,9\} \\ w_o = l + 2 \times (19.6 - 1.86), & o \in \{2,3,10,13,14,15\} \end{cases} \quad . \tag{2.10}$$

After calculating w for each set of winding, all the variables of (2.4) are known and the total magnetic flux density caused by a coil in E core structure is obtained using superposition method:

$$\begin{cases} \vec{B} = \sum_{o=1}^{15} \sum_{i=1}^{N} \vec{B_{i_o}}(l, w_o, d_{i_o}) \\ d_{i_o} = d_o + (i-1) \times 1.86mm \end{cases} \quad . \tag{2.11}$$

In (2.11), d_o is the vertical distance on z-axis between the first turn of each winding and desired point in the space which is $3cm$. Based on Fig.2.8, there are three different values for d_o as there are three rows of winding in two layers of image currents. By knowing the fact that the core center leg length for $E80/38/20$ is $28.2mm$ [38], different values of d_o can be calculated as follows:

$$\begin{cases} d_o = d, & o \in \{1,2,6,7,15\} \\ d_o = d_{15_1} + 2 \times (28.2 - 1.86 \times N), & o \in \{3,4,5,8,14\} \\ d_o = d_{15_1} + 4 \times (28.2 - 1.86 \times N), & o \in \{9,10,11,12,13\} \end{cases} \quad . \tag{2.12}$$

Based on the proposed notation, d_{15_1}, is the last turn of winding number 1 in Fig.2.8. By knowing all the variables, the complete magnetic flux density ,B , at $3cm$ from the structure's surface can be calculated using (2.4), (2.10), (2.11),and (2.12):

$$\vec{B} = \sum_{o=1}^{15} \sum_{i=1}^{15} \vec{B_{i_o}}(l = 20mm, w_o, d_{i_o}) = 1.34 \ \vec{a_z} \ mT \ . \tag{2.13}$$

In the next section FEM simulation is performed on the E core structure to obtain the losses and verify the analytical result from mirror method and Biot-Savart law.

2.3.3 FEM Verification of E Core Structure

In this section, analytical result from (2.13) is verified by Ansys maxwell FEM simulation software. FEM calculated magnetic field at $3cm$ of the structure is $1.54mT$

which leads the computation error of less than 6% which can be reduced by increasing the number of image layers. Ansys calculated conduction loss including all AC losses and core loss for this structure is $3.46W$ and $579mW$ respectively with the applied Lorentz force of $6.15\mu N$ to the sample copper sphere. As expected, due to selection of large core, for a given current, the flux density in the core is lower and core loss per volume is low. Based on the $E80/38/20$ core datasheet, the core loss per volume of E core structure is:

$$\begin{cases} Core\ Volume = 72300\ mm^3 \\ Core\ Loss_{total} = 579\ mW \end{cases} \implies Core\ Loss = 8\ \frac{\mu W}{mm^3}\ . \qquad (2.14)$$
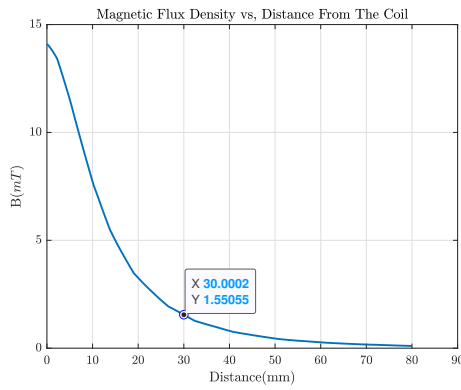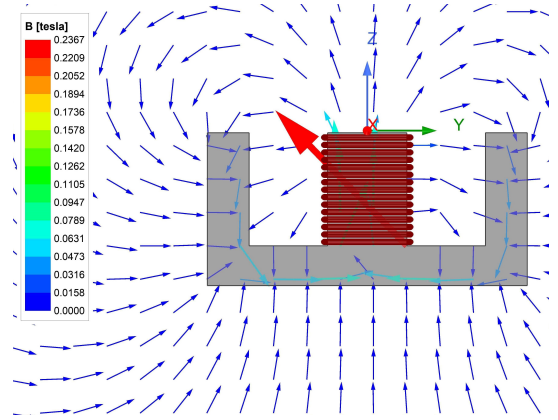
Figure 2.9: Magnetic field of E Core Structure (a) Magnitude with respect to distance (b) Vectors

The magnitude of magnetic field in the space with respect to distance with the core and magnetic field vectors are presented in Fig.2.9. Based on obtained results and comparing the calculated magnetic field with air core structure, adding an E core increased the magnetic flux in the desired distance from $232\mu T$ to $1.54mT$.

After analyzing the effect of large core with single layer winding on maintaining the magnetic field outside the core, the effect of using compact core with concentrated winding configuration is analyzed next. Lower conduction losses and higher core loss per volume is expected for the compact structure with multi layer winding. FEM simulation of concentrated E core structure is presented in the next section.

2.3.4 Concentrated E Core

To determine the effect of core on maintaining the magnetic field outside the core, whole winding area of a compact $E30/15/7$ core is utilized as shown in Fig.2.10. Based on operating frequency of $85kHz$, the core material is the same $3C94$.

The derived analytical model based on mirror method in the previous section is valid for each of winding layers. Concentrated E core structure consists of 3 winding layers with 5 turns in each layer consequently, based on Fig.2.8 there are 14 set of image coils for each layer that adds to the complexity of the analytical calculation. Accordingly, only FEM analysis is considered for the concentrated E core structure although, same as E core structure, the magnetic field can be calculated analytically if needed.
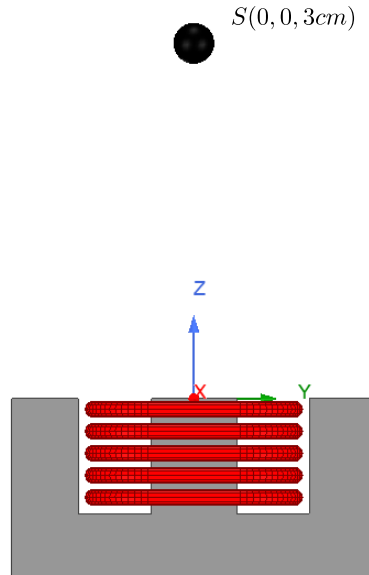
Figure 2.10: Concentrated structure

Magnetic flux Density of Concentrated E Core Structure

Ansys Maxwell FEM based simulation is performed on the concentrated E core structure to obtain the magnetic flux density and complete losses of the structure. Later, it is shown that, the compact structure would not produce adequate magnetic field

in desired coordinates. Based on results from Ansys Maxwell, magnetic flux density at $3cm$ from the coil caused by a $10A$, $85kHz$ sinusoidal current is $305\mu T$ which is a minor improvement compare to the air core structure. Core and complete conduction losses are $293mW$ and $2.63W$ respectively. Also, the applied force is the lowest in concentrated E core structure which is $661.3nN$. The conduction loss is reduced from $3.46W$ to $2.763W$ although, the core loss per volume is increased based on $E/30/15/7$ core volume:

$$\begin{cases} Core\ Volume = 4000\ mm^3 \\ Core\ Loss_{total} = 293\ mW \end{cases} \implies Core\ Loss = 73.25\ \frac{\mu W}{mm^3}\ . \qquad (2.15)$$

The compact core with compact winding configuration cannot maintain the magnetic field outside the structure field As shown in the FEM obtained graph of Fig.2.11. In the compact E core structure compare to large E core structure, the core loss is 9 times higher, conduction loss is 24% lower and the magnetic field in the the desired distance is 5 times lower.
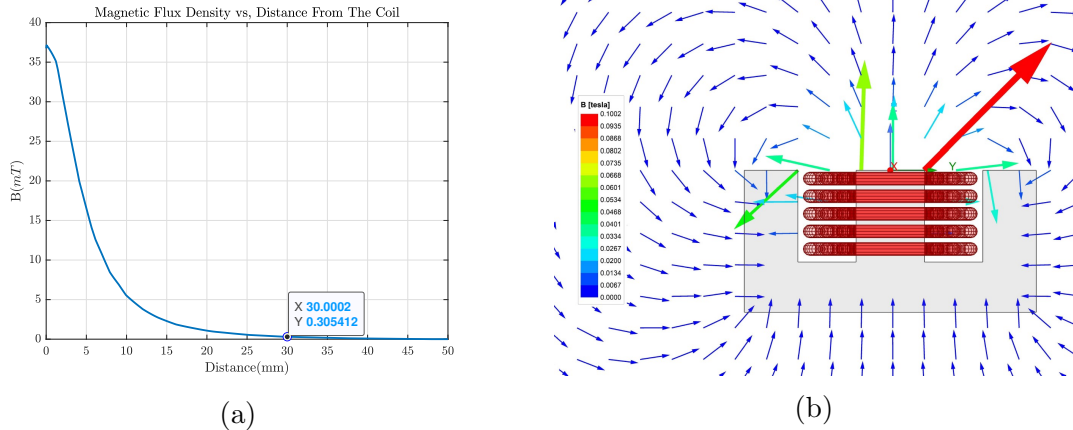
Figure 2.11: Magnetic field of Concentrated Structure (a) Magnitude with respect to distance (b) Vectors

The achieved improvement with adding large E core with single layer winding might not be adequate for repelling small metal particles. A novel secondary coil called, the resonator coil, on top of the original coil with specified distance is placed for further increasing in the magnetic field. Effect of adding second coil is analyzed in the next chapter by analyzing the E core structure with resonator coil.

2.4   E Core with Resonator Coil

It was shown in section 2.3 that adding a large ferrite core to single layer winding of air core structure will improve the magnetic field significantly. In this section, to further improvement the field at the desired point, it is proposed to add a second coil, resonator coil, on top of the single E core structure of the previous section. The second coil does not have to be derived with additional power converter and will only have a capacitor in parallel as shown in Fig.2.14. The combination of the coil, cap and a magnetic field generated by the first coil, will result in a resonance and will amplify the magnetic field between the coils. Fig.2.12 shows the structure of proposed E core structure with resonator coil.
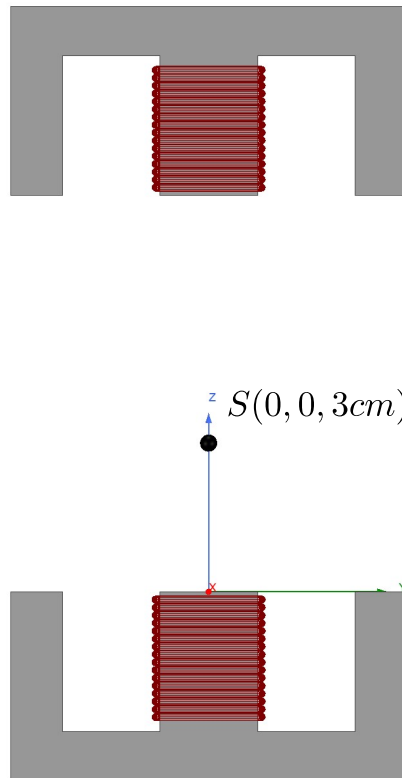
Figure 2.12: E core structure with resonator coil

2.4.1   E Core Structure with resonator coil Variables

To obtain the E core structure with resonator coil variables, the first assumption is that two coils are identical and separated with a pre-define distance. The core material, number of turns and the wire type in the resonator coil, are the same as the main coil. As shown in Fig.2.9, the magnitude of the magnetic flux density is highly sensitive to distance from the coil.

According to Fig.2.9, in a single E core structure, the magnetic field at distances more than $8cm$ from the coil surface is negligible. Consequently, for the E structure with resonator coil, if the gap between the coils is more than $16cm$, the effect of the resonator coil on providing the magnetic field in the desired distance is insignificant. On the contrary, closer coils will have high flux in the middle although, the risk of collision between the scraps and the upper coil is increased as well. Accordingly, distances around $8cm$ is where the resonator coil has advantage and is large enough to let the metal scraps pass through the resonator coil and the main coil. The distance between the lower and upper coil of E structure with resonator coil is considered to be $8cm$ for analysis and FEM simulation purposes. In the next part, the equivalent circuit model of the structure is introduced and the analytical model for calculating the magnetic field is derived.

2.4.2   Modeling of E Core Structure with Resonator Coil

The E structure with resonator coil magnetic field includes two parts: one from the lower coil and the other from the upper or the resonator coil. The modeling and calculation for each coil is similar to simple E structure. After calculating the flux density of each coil, two obtained sinusoidal magnetic fields are added to find the total field between the coils. As a result, the phase angle of magnetic fields is important to calculate the peak, or RMS, value of the total magnetic flux density at the desired coordinates as illustrated in the next section.

Phase effect

Phase angle of magnetic field in both coils, will affect the magnitude and phase of total magnetic field density caused by both coils. Based on Ohm's law for magnetic circuits in (2.16), flux, $\phi(Wb)$ and consequently magnetic flux density, B, are always in phase with their originating current. As a result, the peak value of B occurs at the same phase as the peak value of it's originating current. Fig.2.13 shows that for a 30° lagging current which has its peak value at 120°, the peak value of magnetic flux density is at 120°.

$$\mathscr{F} = Ni = \mathscr{R}\phi \implies I\angle{-30} \rightarrow B\angle{-30} \tag{2.16}$$
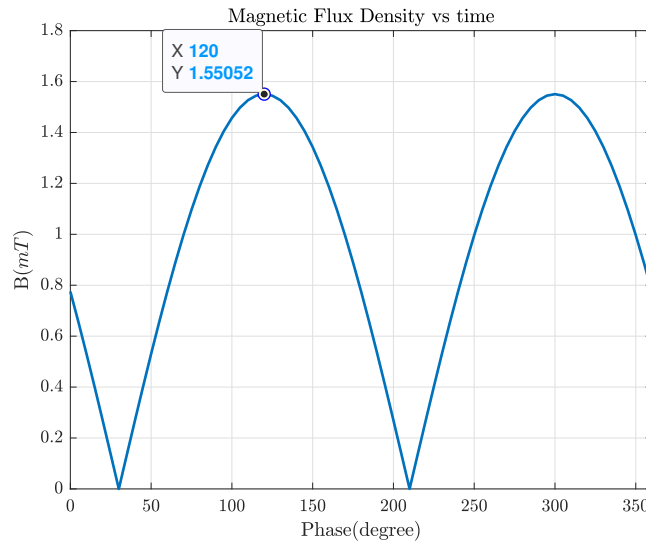
Figure 2.13: Magnitude of magnetic flux density in E core structure at $3cm$ from the coil caused by a 30° lagging current

The phase angle of the magnetic field is the same as the originating current, accordingly, the effect of primary current on phase and magnitude of the secondary coil current should be analyzed next. The E structure with resonator coil is similar to a $1:1$ transformer with a huge air gap and very small magnetizing inductance, L_m. As a result, equivalent circuit for this structure is similar to a transformer's T-model as shown dotted in Fig.2.14.
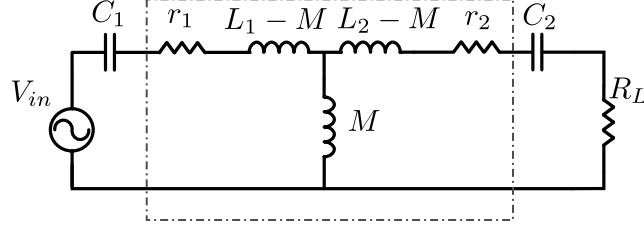
Figure 2.14: Equivalent circuit model of E structure with resonator coil

In general, self inductance of each side is unique although, for symmetrical structures as E with resonator coil, both self inductances, L_1 and, L_2 are equal. Based on E core structure with resonator coil and $3C94$ $E80/38/20$ core, FEM calculated parameters are $33.6\mu H$ and $399.6nH$ for L_1 and M respectively. To cancel the primary inductance, C_1 can be added in the resonance frequency of the primary side leakage inductance :

$$C_1 = \frac{1}{(L_1 - M)(2\pi f_{operation})^2} = 105.5 \ nF \ . \tag{2.17}$$

Based on equivalent circuit presented in Fig.2.14, magnitude and phase of the secondary current can be regulated with respect to the primary current by adding C_2 and R_L. Inductance's resistor are negligible and R_L is the only resistor that contributes in calculations. Magnitude and phase of current in the resonator coil can be written as a function of the primary current and circuit parameters:

$$\begin{cases} I_M Z_m = I_2(Z_{L_1-M} + Z_{C_2} + R_L) \\ I_1 = I_m + I_2 \end{cases} \tag{2.18}$$

$$\implies I_2 = \frac{Z_M}{Z_{L_1-M} + Z_{C_2} + R_L + Z_M} I_1$$

Based on (2.18), assuming $10A$ injecting current for the primary side, Fig.?? shows some contour plots of possible magnitudes and phases for the secondary current caused by regulation of C_2 and R_L. One can see that, secondary current can be regulated to any phase and magnitude, as the values are shown with number tags on the graph, by choosing proper R_L and C_2 value.

c After obtaining the phase and magnitude of the secondary current based on the primary side current, superposition method can be used to obtain the magnetic flux density caused by both coils from the following equation:

$$\vec{B} = \vec{B_{Down}} + \vec{B_{Up}} = \vec{B_1} I_1 \sin(\omega t) - \vec{B_2} I_2 \sin(\omega t - \theta_2) . \tag{2.19}$$

By defining M as:

$$M = \sqrt{(B_1 I_1)^2 + (B_2 I_2)^2 + 2 B_1 B_2 I_1 I_2 \cos(\theta_2)} \tag{2.20}$$

The magnetic field formula can be rewritten as:

$$\vec{B} = M \sin\left(\omega t - \arcsin\left(\frac{B_2 I_2 sin\,(\theta_2)}{M}\right)\right) . \tag{2.21}$$

According to (2.21), the lagging curve angle of the secondary current can have the positive or negative affect on the magnetic field. To obtain the maximum value of the magnetic field the derivative of magnitude, M, with respect to θ_2 is calculated:

$$\frac{\partial M}{\partial \theta_2} = 0 \implies -\frac{B_1 B_2 I_1 I_2 sin\,(\theta_2)}{\sqrt{(B_1 I_1)^2 + (B_2 I_2)^2 + 2 B_1 B_2 I_1 I_2 \cos(\theta_2)}} = 0 \tag{2.22}$$

$$\implies \theta_2 = 0° \ or \ 180°$$

According to (2.21) and (2.22), the resonator coil would have negative effect if current phases are the same. As a result, the magnetic field in the middle is zero for equal current magnitudes and phases. However, with 180° phase difference, the resonator coil will have the maximum effect in maintaining the field between the coils and doubles it in the middle. By knowing the possibility of secondary current regulation, and based on the derived model for calculating the magnetic field density of the E core structure, next step is calculating the magnetic field of E core structure with resonator coil using the superposition method.

Magnetic flux Density Calculation of E core with Resonator Coil

Phase and magnitude of resonator coil is needed prior to calculation of the magnetic field. To compare the E core with resonator coil with previous structures, current

of both coils is assumed to be the same $10A$ with $180°$ phase difference with the primary current to use the full potential of the resonator coil. Based on the concept of image currents introduced in chapter 2.3, and derived formula for calculating the magnetic field of an E core, (2.11), the magnitude of B in $3cm$ from the main coil, and consequently $5cm$ from the resonator coil is obtained.

$$(2.11) \implies \vec{B_{Total}} = \vec{B_{Down}} + \vec{B_{Up}} = \vec{B}(20, 30, 15) + \vec{B}(20, 50, 15) = 1.78 \ \vec{a_z} \ mT$$

$$(2.23)$$

2.4.3   FEM Verification

Based on the simulated model in the Ansys Maxwell software, magnetic field in $3cm$ of the main coil is $2.06mT$ as shown in Fig.2.15 which is less than 15% computation error with respect to the calculated $1.78mT$ that can be reduced considering more mirror layers. The obtained Lorentz force for the E core structure with the resonator coil is $7.03\mu N$. The obtained conduction and core losses from Maxwell are $6.80W$ and $1.04W$ respectively and is almost two times higher than E core structure as there are two cores.

As expected, resonator coil improved the magnetic flux strength between the coils significantly and doubled the flux at $4cm$ of both coils, from $0.9mT$ in Fig.2.9 to $1.8mT$ in E core structure with resonator coil with the cost of doubling both conduction and core losses.

The core loss is related to core volume and increasing the working length to $20cm$ costs 9 extra $E80/38/20$ cores for each coil. Consequently, ten times more material leads to the increase in the core loss and accordingly a drop in the efficiency. To achieve the best structure, the core volume should be reduced without loosing magnetic flux strength in between the two coils. The core is responsible for focusing the flux in the desired coordinates, which can be translated to a higher magnetic flux density and higher induced force on the particle.
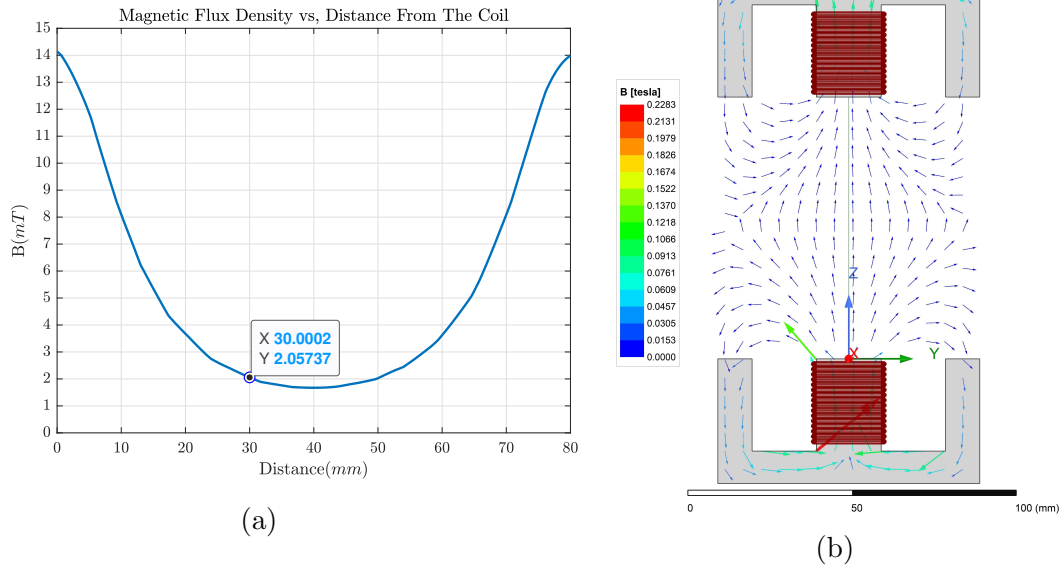
Figure 2.15: Magnetic field of E core structure with resonator coil (a) Magnitude with respect to distance (b) Vectors

A new category of static separators that is based on planar magnetic structure is proposed in the next chapter that uses a compact and flat concentric turns instead of conventional coils with core sticks located beneath the winding. It is shown that this planner structure will eliminate the drawbacks of the non-planar structure while improving the magnetic field at the desired coordinates. Later, it is shown that planar structures can provide higher force with less input power while having lower total loss to separate the non-ferrous metal particles.

2.5   Summary

To design a static separator, the most simple structure that is an air core coil is first analyzed and modeled using the Biot-Savart law and then verified by FEM based analysis using Ansys Maxwell software. To observe the effect of a core, a simple E ferrite core is added to the structure to improve the magnetic field outside the core. Two cases of large and compact cores were analyzed and it is shown that larger core provides better results in maintaining the magnetic field outside the core. A second

37

coil connected to a capacitor is added that would resonate with the first coil and proved to further improve the flux density. Based on the equivalent circuit model, the effect of the second coil is analyzed.

Chapter 3

Proposed Planar Magnetic Structure Development

In this chapter, a novel planar based structure with concentric turns and core sticks is proposed for recycling non-ferrous metals. The working principle of the proposed planar separator is similar to non-planar structures and is based on the applied Lorentz force to non-ferrous metal particles. To increase the applied force, the produced magnetic field from the structure should be maximized. The detailed analysis of the sample structure, which is shown in Fig.3.1, is provided to compare the magnitude of flux density and losses in planar separator with E core based structures.
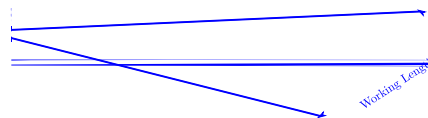
Figure 3.1: Structure of proposed single coil planar structure with core sticks

The design and optimization of the proposed structure without cores is provided using Biot-Savart law, and analytical calculations and then the results are verified

by FEM calculation using Ansys Maxwell software. Core bars are added to the structure to increase the magnetic flux density with reasonable core loss. The new mirror method based on the weighted average of two modified mirror methods is used to model the proposed structure. A novel resonator coil with different design variables is added to the structure for further improvement in maintaining the magnetic field. Similarly, all of the analytical models are verified by Ansys Maxwell software.

A comprehensive FEM based comparison is conducted for three different scenarios; same input power, same applied force and, same magnitude flux density at the specific. The comparisons are presented for non-planar and the proposed planar structure with different core coverage.

3.1 Proposed Planar Structure Details and Assumptions

The proposed structure utilizes concentric turns and three core sticks located in the middle and far sides of the structure beneath the winding as shown in Fig.3.1. The rectangular window area in the middle of winding, the window area, is the working region of the structure. It is shown that in narrower window area, the magnetic flux density is higher although, implementing narrow gap is challenging and also due to high speed of feeder's belt, the force may not apply to the particles. Consequently, the working region should be wide enough to provide adequate working surface on the feeder's belt with minimum compromise in the magnitude of magnetic flux density. The length of the window area is the working length of the structure which is reduced by increasing the number of turns in a fixed length structure.

Unlike non-planar structures, the proposed planar system is very versatile with various design parameters to achieve the highest magnetic field in the desired coordinates that is $3cm$ from the structure's surface. design parameters includes working length and width which determines the dimensions of window area in the coil. The structure curve angle is another parameter which affects the magnitude of magnetic

40

flux density in the space.

For simplicity, %80 scaled down structures with working length of $20cm$ is used as shown in fig.3.2. Three main categories of planar structures: Air-core, single winding bar shaped core, bar shaped core structure with resonator coil is analyzed.
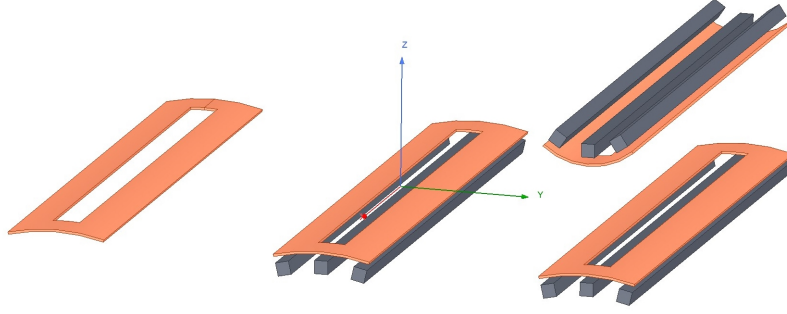
Figure 3.2: Proposed structure with 15 turns of predefined Litz wire, 30° curve angle and $1m$ working length

To achieve comparable results with non-planar structures, same operating conditions are assumed for all the planar structures. The injecting current is $10A$, $85kHz$ sinusoidal current and the wire is set $1.76mm - 180 \times AWG38$ Litz wire similar to other structures studied in the previous chapters. The number of turns is 15 and the window area dimensions is set at $2cm^2$ square to match the non-planar structures working region. The magnetic flux density at $3cm$ from the structure is used as a reference for the comparison between different structures. Similarly, a $3mm$ copper sphere is considered as a test object for obtaining the applied Lorentz force caused by the proposed structure from Ansys Maxwell.

3.2 Proposed Air Core Structure

First structure in the planar structures is Air core structure as shown in Fig.3.3. The curve angle can be used as an extra degree of freedom in the design of the proposed planar structure. The curve angle, φ, may vary between 0° and 180°. The optimum value of this variable is found later however, at this point, the φ is set at 30° for the

sake of analysis.
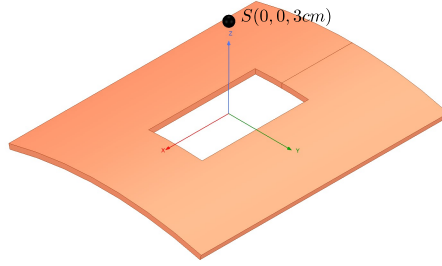
Figure 3.3: Air core planar structure with 30° curve angle

3.2.1 Modeling of Air Core Structure

Each rectangular turns of the proposed planar structure consists of four parts: two straight wires 1,3 and two curved wires 2,4 as shown in Fig.3.4. The origin of the coordinate system is set at the middle of working area as shown in Fig. 3.4.
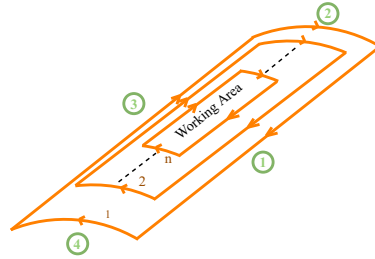
Figure 3.4: Diagram of proposed structure with n turns

Side Wires Magnetic Field Calculation

To model the proposed planar structure, each turn of the winding is divided in four parts, two straight wires at the side and two curved parts at front and rear ends. Then, the magnetic flux density generated by each turn can be found by superposition of fields generated by each part. Line Biot-Savart law in (2.3) is used to calculate the field at any arbitrary point in the space, S, caused by a straight current carrying finite wire, located at an arbitrary location alongside x-axis from $-x_j$ to x_j as shown in Fig.3.5.
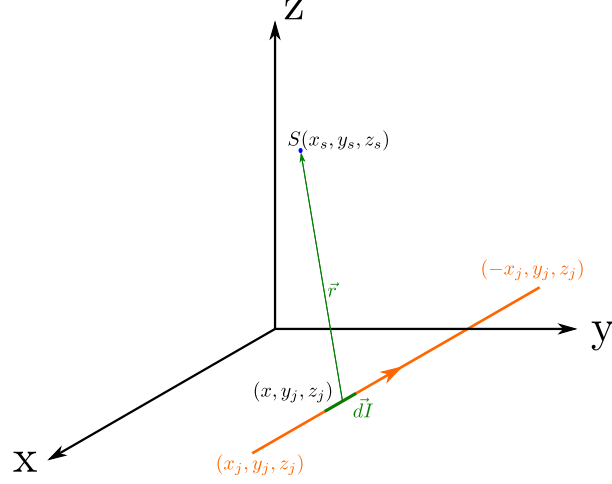
Figure 3.5: Current carrying wire in arbitrary location along x-axis

The magnitude of distance vector, r, is needed to calculate the integral in (2.3). Based on coordinates of desired location in space, S, and current element, I, in Fig.3.5, distance vector can be obtained:

$$\vec{r} = S - dI = (x_s - x)\vec{a_x} + (y_s - y_j)\vec{a_y} + (z_s - z_j)\vec{a_z} \implies$$

$$|\vec{r}| = \sqrt{(x_s - x)^2 + \underbrace{((y_s - y_j)^2 + (z_s - z_j)^2)}_{\alpha^2}} = \sqrt{(x_s - x)^2 + \alpha^2} \ . \tag{3.1}$$

The current element vector is along x-axis with magnitude of I, as a result, dI is:

$$\vec{I} = \vec{dI} = I\vec{dl} = -Idx \ \vec{a_x} \ . \tag{3.2}$$

According to (3.2), the cross product in (3.1) is:

$$\vec{dI} \times \vec{r} = I(z_s - z_j) \ \vec{a_y} - I(y_s - y_j) \ \vec{a_z} \ . \tag{3.3}$$

By obtaining $\vec{dI}$ and $\vec{r}$, magnetic field density, B, of the straight wire can be calculated using the line Biot-Savart equation in (2.3).

$$\xrightarrow[(3.1)]{(2.3)} \vec{B} = \frac{\mu_0 I}{4\pi} \int_{-x_j}^{x_j} \left[\frac{(z_s - z_j)}{((x_s - x)^2 + \alpha^2)^{\frac{3}{2}}} \ \vec{a_y} - \frac{(y_s - y_j)}{((x_s - x)^2 + \alpha^2)^{\frac{3}{2}}} \ \vec{a_z} \right] dx$$

$$= \frac{\mu_0 I}{4\pi\alpha^2} \left[(z_s - z_j) \left(\frac{(x_s - x_j)}{\sqrt{(x_s - x_j)^2 + \alpha^2}} - \frac{(x_s + x_j)}{\sqrt{(x_s + x_j)^2 + \alpha^2}} \right) \vec{a_y} \right. \tag{3.4}$$

$$\left. + (y_s - y_j) \left(\frac{(x_s - x_j)}{\sqrt{(x_s - x_j)^2 + \alpha^2}} - \frac{(x_s + x_j)}{\sqrt{(x_s + x_j)^2 + \alpha^2}} \right) \vec{a_z} \right]$$

Front and Rear Curved Wires Magnetic Field Calculation

Calculating magnetic flux density caused by a curve wire in any arbitrary point in the space is complicated, except for points located along the curve center axis. Because of the term r^3 in (2.3), using Biot-Savart integral is difficult for non-conventional shapes similar to partial curve in the proposed structure. To simplify the Biot-Savart equation, new magnetic variable, magnetic vector potential, A, is introduced prior to the calculation of the magnetic flux density generated by a curved wire.

- Magnetic Vector Potential ($A(Tm)$):   In calculus, the divergence of any vector like F, which is $\nabla \cdot F$, is the net outflow of vector field F from an arbitrary point in the space. There is no source or sink for the magnetic field, as a result the net overflow of magnetic field for any point in the space is zero:

$$\nabla \cdot B = 0 \ . \tag{3.5}$$

This is referred as Gauss's law in magnetic field. In mathematics, divergence of the curl of any arbitrary vector like A, is zero:

$$\nabla \cdot (\nabla \times A) = 0 \ . \tag{3.6}$$

Combining (3.6) with Gauss law in the magnetic field in (3.5) results in the definition of an auxiliary magnetic field, A, which is called the magnetic vector potential [29]:

$$B = \nabla \times A \ . \tag{3.7}$$

Divergence of A is defined as zero to complete the definition of the new vector:

$$\nabla \cdot A = 0 \tag{3.8}$$

After defining the new vector, an analytical formula for obtaining the magnetic vector potential is derived using the Amperes law:

$$\oint_c H \cdot dl = I_{enclosed} \ . \tag{3.9}$$

44

Based on Stokes theorem any line integral of an arbitrary vector, F, around the boundary of a surface can be written as the surface integral of the curl of the same vector:

$$\oint_c F \cdot dl = \int_s (\nabla \times F) \cdot ds \qquad (3.10)$$

Stokes theorem in (3.10) can be applied to the amperes law (3.9):

$$\begin{cases} \oint_c H \cdot dl = \int_s (\nabla \times H) \cdot ds = I_{enclosed} \\ \\ I_{enclosed} = \int_s J \cdot ds \end{cases} \implies \nabla \times H = J . \qquad (3.11)$$

This formula can be rewritten in terms of B and the permeability of the surrounding medium which is free space:

$$\nabla \times B = \mu_0 J . \qquad (3.12)$$

Magnetic vector potential can be added to the equation by substituting (3.7) in (3.12):

$$\nabla \times (\nabla \times A) = \mu_0 J . \qquad (3.13)$$

Curl of the curl of any vector can be rewritten as:

$$\nabla \times (\nabla \times A) = \nabla(\nabla \cdot A) - \nabla^2 A . \qquad (3.14)$$

Based on the definition of A in (3.8), $\nabla(\nabla \cdot A) = 0$. Consequently, (3.12) can be rewritten as:

$$\nabla^2 A = -\mu_0 J . \qquad (3.15)$$

Analytical formula for calculating A, is obtained by solving (3.15):

$$A = \frac{\mu_0}{4\pi} \int_v \frac{J \, dv}{R_s} . \qquad (3.16)$$

In (3.16), v is the volume enclosing the current density, J, which originates the magnetic vector potential, A, and R_s is the magnitude of the vector which connects differential volume of the current containing J to the desired point. To simplify the

equation, in a wire with uniformly distributed current over the volume, total current is:

$$J \, dv = J \, ds \, dl \quad \overset{Jds=I}{\Longrightarrow} \quad J \, dv = I \, dl \tag{3.17}$$

Uniformly distributed current in (3.17), will simplify the volume integral in (3.16) to a line integral along wires path:

$$A = \frac{\mu_0}{4\pi} \int_l \frac{I}{R_s} \, dl \tag{3.18}$$

Based on (3.18), A in any point, is in the direction of it's source current. In non-conventional shapes similar to partially curved wires, Biot-Savart equation in (2.3) is obtained by calculating curl of A in (3.18).

To calculate the magnetic vector potential of a partially curved wire which is shown in Fig.3.6, spherical coordinates are used to reduce the computation complexities. The integral in (3.16) cannot be solved analytically for any arbitrary point [29]. As such, it is assumed that, the desire point, S, is located at $y = 0$ plane.
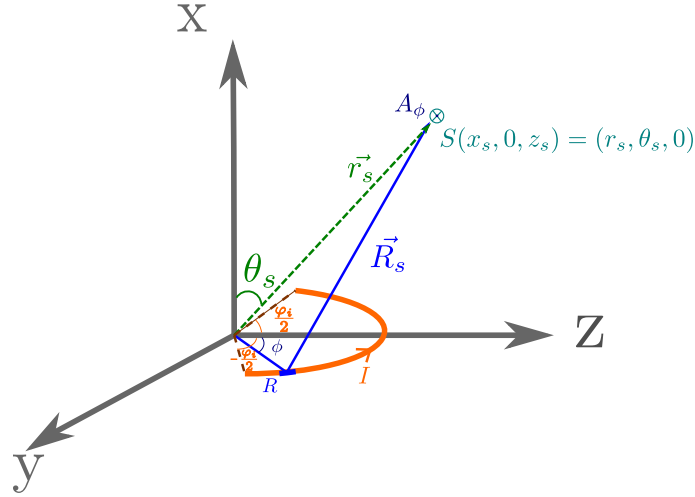
Figure 3.6: Curve wire and an arbitrary point is xz-plane

Magnetic vector potential direction is the same as the originating current and according to Fig.3.6, A, is in ϕ direction in spherical coordinates. The magnitude of vector $|\vec{R}_s|$ in Fig.3.6 should be calculated prior to the calculation of the magnetic

vector potential's integral:

$$\vec{R_s} = \vec{r_s} - \vec{R} \ . \tag{3.19}$$

According to Fig.3.6:

$$\begin{cases} \vec{r_s} = r_s \cos(\theta_s) \ \vec{a_x} + r_s \sin(\theta_s) \ \vec{a_z} \\ \\ \vec{R} = R \sin(\phi) \ \vec{a_y} + R \cos(\phi) \ \vec{a_z} \end{cases} . \tag{3.20}$$

Magnitude of R_s can be calculated by substituting (3.20) in (3.19):

$$\vec{R_s} = \vec{r_s} - \vec{R} = r_s \cos(\theta_s) \ \vec{a_x} - R \sin(\phi) \ \vec{a_y} + (r_s \sin(\theta_s) - R \cos(\phi)) \ \vec{a_z}$$

$$. \tag{3.21}$$

$$\implies R_s = \sqrt{r_s^2 + R^2 - 2 r_s R \sin(\theta_s) \cos(\phi)}$$

The value of r_s and θ_s can be calculated using S coordinates:

$$\begin{cases} r_s = \sqrt{x_s^2 + z_s^2} \\ \theta_s = \arctan(\frac{z_s}{x_s}) \end{cases} . \tag{3.22}$$

The other variable which is involved in the calculation of the magnetic vector potential in (3.16) is dl which is in ϕ direction:

$$dl = R \cos(\phi) \ d\phi \tag{3.23}$$

Last step would be defining the limits of integral which is curve angle of the wire. According to Fig.3.6, limits of integral are from $-\frac{\varphi_i}{2}$ to $\frac{\varphi_i}{2}$. Replacing (3.21) and (3.23) in (3.16) will shape the magnetic vector potential formula:

$$A_{\phi S} = \frac{\mu_0 I}{4\pi} \int_{-\frac{\varphi_i}{2}}^{\frac{\varphi_i}{2}} \frac{r_s \cos(\phi)}{\sqrt{r_s^2 + R^2 - 2 r_s R \sin(\theta_s) \cos(\phi)}} \ d\phi$$

$$\tag{3.24}$$

$$= \frac{\mu_0 I}{2\pi} \int_{0}^{\frac{\varphi_i}{2}} \frac{r_s \cos(\phi)}{\sqrt{r_s^2 + R^2 - 2 r_s R \sin(\theta_s) \cos(\phi)}} \ d\phi$$

New variable, γ, is introduced for solving the (3.24) variable changing technique:

$$\gamma = \frac{\pi}{2} - \frac{\phi}{2} \implies \begin{cases} d\phi = -2 d\gamma \\ \cos(\phi) = -\cos(2\gamma) = 2\sin^2(\gamma) - 1 \end{cases} \tag{3.25}$$

47

In (3.24), ϕ is replaced with the new variable γ and according to (3.22), r_s^2 and $r_s \sin(\theta_s)$ can be replaced with z_s and $x_s^2 + z_s^2$ respectively for further simplification of the magnetic vector potential formula:

$$A_{\phi S} = \frac{R\mu_0 I}{\pi} \int_{\frac{\pi}{2} - \frac{\varphi_i}{4}}^{\frac{\pi}{2}} \frac{2\sin^2(\gamma) - 1}{\sqrt{(R + z_s)^2 + x_s^2 - 4Rz_s \sin^2(\gamma)}} \, d\gamma \qquad (3.26)$$

If new variable k define as:

$$k = \sqrt{\frac{4Rz_s}{(R + z_s)^2 + x_s^2}} \qquad (3.27)$$

then (3.26) can be rewritten as:

$$A_{\phi S} = \frac{\mu_0 I}{\pi k} \sqrt{\frac{R}{z_s}} \left[\left(1 - \frac{k^2}{2}\right) \left(\int_{\frac{\pi}{2} - \frac{\varphi_i}{4}}^{\frac{\pi}{2}} \frac{d\gamma}{\sqrt{1 - k^2 \sin^2(\gamma)}} \right) \right.$$

$$\left. - \left(\int_{\frac{\pi}{2} - \frac{\varphi_i}{4}}^{\frac{\pi}{2}} \sqrt{1 - k^2 \sin^2(\gamma)} \, d\gamma \right) \right] \qquad (3.28)$$

The two integral in (3.28) are called elliptical integral of first and second kind where are related functions defined as the value of certain integrals. Elliptical integrals first arose in connection with the problem of finding the arc length of an ellipse and cannot be expressed as elementary functions but can be rewritten as one of three main forms known as three Legendre canonical forms. Incomplete elliptic integral of first kind, F is defined as:

$$F(\varphi, k) = F(\varphi | k^2) = \int_0^\varphi \frac{d\theta}{\sqrt{1 - k^2 \sin^2(\theta)}} \qquad \varphi \leq \frac{\pi}{2} \ . \qquad (3.29)$$

Elliptic integrals are be complete when $\varphi = \frac{\pi}{2}$ and consequently, complete elliptic integral of first kind is $F(k) = F(\frac{\pi}{2}, k)$. Incomplete elliptic integral of the second kind is defined as:

$$E(\varphi, k) = E(\varphi | k^2) = \int_0^\varphi \sqrt{1 - k^2 \sin^2(\theta)} \, d\theta \qquad \varphi \leq \frac{\pi}{2} \ . \qquad (3.30)$$

Again, $E(\frac{\pi}{2}, k) = E(k)$ is the complete integral of the second find which gives the arc length of an ellipse. At last, incomplete elliptical integral of third kind is defined as

follows:

$$\Pi(n; \varphi, k) = \Pi(n; \varphi|k^2) = \int_0^\varphi \frac{1}{\sqrt{1 - n\sin^2(\theta)}} \frac{d\theta}{\sqrt{1 - k^2\sin^2(\theta)}} \qquad \varphi \leq \frac{\pi}{2} \ . \qquad (3.31)$$

Complete integral of the third kind has the same definition as the first and second. By introducing elliptical integrals one can see that, (3.28) is expressed as a linear function of elliptic integrals of the first and second kind:

$$A_{\phi_S} = \frac{\mu_0 I}{\pi k} \sqrt{\frac{R}{z_s}} \left[\left(1 - \frac{k^2}{2}\right) \left(F(k) - F(\frac{\pi}{2} - \frac{\varphi_i}{4}|k)\right) \right. \\ \left. - \left(E(k) - E(\frac{\pi}{2} - \frac{\varphi_i}{4}|k)\right) \right] \qquad (3.32)$$

Based on the definition of A in (3.7), magnetic field density, B, can be obtained by calculating the curl of magnetic vector potential at S. According to curl operator features, B_ϕ is zero. Curl of A can be calculated in cylindrical coordinates to obtain $\vec{B}$:

$$\vec{B} = \vec{\nabla} \times \vec{A} \implies \begin{cases} B_\rho = -\dfrac{\partial A_\phi}{\partial z} \\ \\ B_z = \dfrac{1}{\rho}\dfrac{\partial(\rho A_\phi)}{\partial \rho} \end{cases} \qquad . \qquad (3.33)$$

Based on the orientation of the main coordinate system in Fig.3.6, the transformation from cylindrical to Cartesian coordinates is based on the following table:

Table 3.1: Transformation

Cylindrical	Cartesian
z	x
ρ	$\sqrt{z^2 + y^2}$
$\rho\cos(\phi)$	z
$\rho\sin(\phi)$	y

Accordingly:

$$B_\phi = 0 \implies B_{y_{cartesian}} = 0 \implies \begin{cases} B_\rho = B_{z_{cartesian}} \\ B_z = B_{x_{cartesian}} \end{cases} \qquad (3.34)$$

Based on (3.32) to (3.34) magnetic field density caused by a curved wire can be calculated:

$$B_\rho = B_{z_{cartesian}} = \frac{\mu_0 I x_s}{2\pi z_s \sqrt{(R+z_s)^2 + x_s^2}} \left[-\left(F(k) - F(\frac{\pi}{2} - \frac{\varphi_i}{4}|k)\right) \right.$$

$$\left. + \left(\frac{R^2 + z_s^2 + x_s^2}{(R-z_s)^2 + x_s^2}\right) \left(E(k) - E(\frac{\pi}{2} - \frac{\varphi_i}{4}|k)\right) \right] \tag{3.35}$$

and

$$B_z = B_{x_{cartesian}} = \frac{\mu_0 I}{2\pi \sqrt{(R+z_s)^2 + x_s^2}} \left[\left(F(k) - F(\frac{\pi}{2} - \frac{\varphi_i}{4}|k)\right) \right.$$

$$\left. + \left(\frac{R^2 - z_s^2 - x_s^2}{(R-z_s)^2 + x_s^2}\right) \left(E(k) - E(\frac{\pi}{2} - \frac{\varphi_i}{4}|k)\right) \right] \tag{3.36}$$

The obtained analytical formula for calculating curve wire magnetic field will conclude the modeling of proposed structure. In the next section, by using the superposition method and combining (3.4) with (3.35) and (3.36) total magnetic field caused by the proposed planar structure is obtained.

3.2.2 Magnetic Field Calculation of the Proposed Planar Structure

The total magnetic field of the proposed structure is the summation of each turn magnetic flux density which can be obtained from (3.4) for the side part and from (3.35) and (3.36) for the curved part of each turn. The magnitude of magnetic field at $3cm$ from the structure is calculated and accordingly, S coordinates is $(0, 0, 3cm)$. Next step would be obtaining the variables of (3.4), (3.35) and, (3.36) should be for each turn of the winding. According to Fig.3.37 for a planar structure with N turns and window area of $h \times H$, in flat non-curved state, by assuming d for wire diameter, structures dimensions in flat state is:

$$\begin{cases} w = h + N \times d \\ L = H + N \times d \end{cases} \tag{3.37}$$

Where w and L are half width and length of the structure respectively.
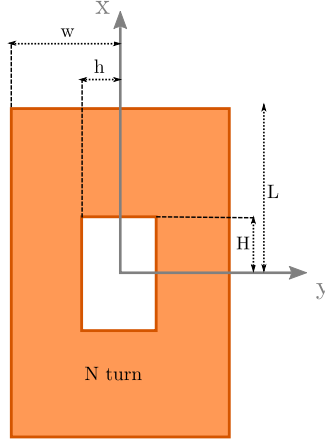
Figure 3.7: Flat Planar structure with N turn winding diagram

Curved structure with the curve angle of $\varphi\ rad$, is part of a cylinder with the radius of R and height of $2L$. The arc length of the curve is total width of the structure in flat state, $2w$, and accordingly cylinder radius, R, can be calculated using the arc length formula:

$$R = \frac{2w}{\varphi} \ .$$ (3.38)

The curve radius is the same for all the turns although, the width and curve angle is different. According to the wire diameter, d, total width and length of the $i-th$ turn can be calculated as follows:

$$\begin{cases} w_i = w - (i-1)d \\ L_i = L - (i-1)d \end{cases} \ .$$ (3.39)

The arc length formula can be used to calculate the curve angle of the ith turn with the radius of R and the total width from (3.40):

$$\varphi_i = \frac{2w_i}{R} \ .$$ (3.40)

The end points of ith turn of the structure is presented in Fig.3.8. Each turn is divided in four parts and x_{j_i} is the x element of jth part of the ith turn.
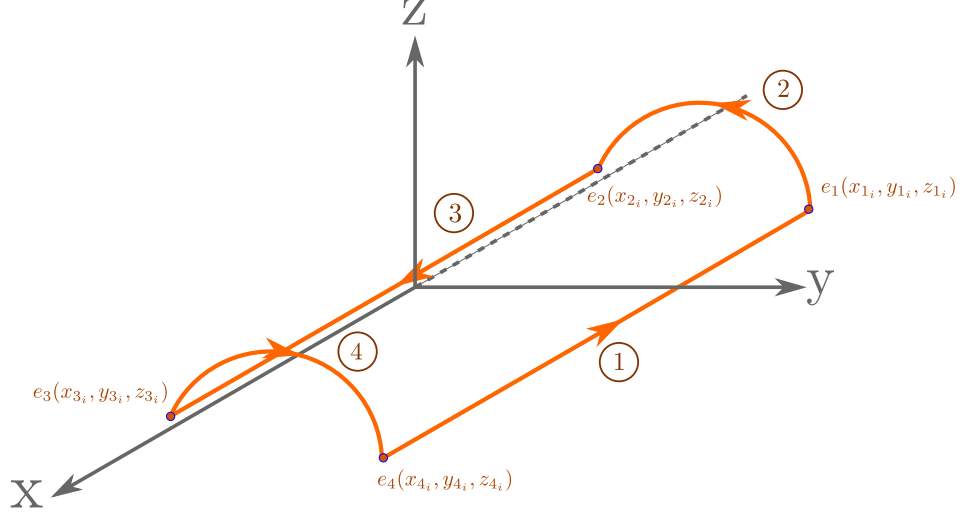
Figure 3.8: Complete one turn of proposed planar structure with end points

Based on the origin of the selected coordinate system which is located at the middle of the structure, x element of the end points in the ith turn is:

$$\begin{cases} x_{1_i} = x_{2_i} = -\big(L - (i-1)d\big) \\ \\ x_{3_i} = x_{4_i} = L - (i-1)d \end{cases} . \tag{3.41}$$

According to the side view of the ith turn presented in Fig.3.9, y and z element of the endpoints can be obtained using the features of arc and right triangle. As shown in Fig.3.9, C_i is the origin of the curve and $|C_iE_i|$ is equal to the curves radius which is R from (3.38). Consequently, $|C_iF_i|$ and $|F_iE_i|$ can be calculated using the trigonometric functions in $C_i\overset{\triangle}{E}_iF_i$ right triangle with the angle of $\dfrac{\varphi_i}{2}$:

$$\begin{cases} |C_iF_i| = R\cos(\frac{\varphi_i}{2}) \\ \\ |F_iE_i| = R\sin(\frac{\varphi_i}{2}) \end{cases} . \tag{3.42}$$

$|F_iE_i|$ is the horizontal distance from an endpoint to the origin of the coordinate system which is y element of the endpoint. To acquire the z element of the endpoint, $|OF_i|$ should be calculated which can be done using $|C_iF_i|$ in (3.42):

$$|OF_i| = |OC_i| - |C_iF_i| = R(1 - \cos(\frac{\varphi_i}{2})) . \tag{3.43}$$
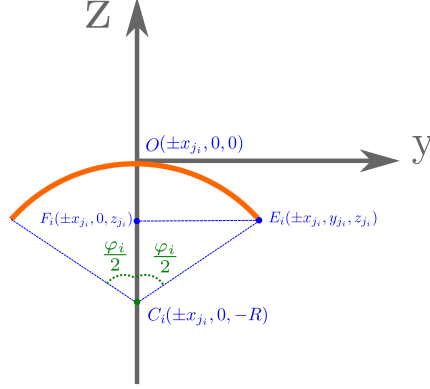
Figure 3.9: Curved part of the winding in $i - th$ turn in yz plane

According to (3.42) , (3.43) and, Fig.3.8, y and z element of the endpoints are:

$$\begin{cases} z_{j_i} = -|OF_i| = R(\cos(\frac{\varphi_i}{2}) - 1) \\ \\ y_{1_i} = y_{4_i} = -y_{2_i} = -y_{3_i} = |F_iE_i| = R\sin(\frac{\varphi_i}{2}) \end{cases} \qquad (3.44)$$

Coordinates of the endpoint is calculated using (3.41) and (3.44) and the magnetic field caused by four sections of each turn would form the complete turn field. According to Fig.3.8, current values are:

$$\begin{cases} I_1 = I_2 = I \\ I_3 = I_4 = -I \end{cases} \qquad (3.45)$$

Total magnetic field of the structure at the desire point, S, located at $(0, 0, 3cm)$ is calculated next. In each turn, magnetic field caused by side wires, B_1 and B_3, and curved wires, B_2 and B_4 will form the total flux density of the turn. The magnetic field of the straight wires is calculated using (3.4) and according to (3.44), (3.45) and, S coordinates the magnetic field from side wires is along the $z - axis$.

$$\begin{cases} y_{1_i} = -y_{3_i} \\ I_1 = -I_3 \\ B_{side_i} = B_{1_i} + B_{3_i} \end{cases} \overset{(3.4)}{\implies} \begin{cases} \vec{B}_{x1_i} = -\vec{B}_{x3_i} \\ \vec{B}_{z1_i} = \vec{B}_{z3_i} \end{cases} \qquad (3.46)$$

Accordingly, the magnetic field from the $i - th$ turn side wire is:

$$B_{1_i} = B_{3_i} \implies B_{side_i} = 2B_{1_i} = \frac{\mu_0 I}{2\pi\alpha_i^2}\left(\frac{x_{1_i}y_{1_i}}{\sqrt{x_{1_i}^2 + \alpha_i^2}}\right) \vec{a_z} , \qquad (3.47)$$

in which:

$$\alpha_i = \sqrt{y_{1_i}^2 + (z_s - z_{1_i})^2)} \; . \tag{3.48}$$

The magnetic field from the side part of the $i-th$ turn is presented in (3.47). To complete the analytical modeling of the proposed structure, magnetic field of curved part for the $i-th$ turn, which is presented in Fig.3.10, is obtained from(3.35) and (3.36).
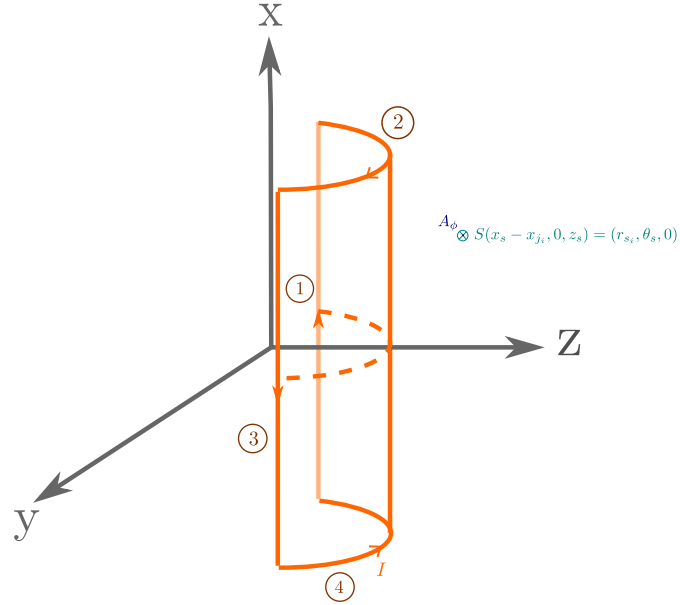
Figure 3.10: side view of complete one turn of the proposed structure

In order to calculate the magnetic flux density of the curved wire, according to Fig.3.6 and the analytical process in section 3.2.1 which leads to (3.35) and (3.36), the origin of the coordinate system should be relocated to the curved wire origin and accordingly with respect to the origin of main coordinate system, O_1 presented in Fig.3.10, the origin of new coordinate systems for each turn O_{2_i} and O_{4_i}, for calculating the magnetic field of cured part is:

$$\overset{(3.40)}{\Longrightarrow} \begin{cases} O_{2_i} = (L_i, 0, 0) \\ O_{4_i} = (-L_i, 0, 0) \end{cases} \quad with \; respect \; to \; O_1 \tag{3.49}$$

and accordingly the coordinates of the S in new coordinate systems is:

$$\begin{cases} x_{S_{j_i}} = x_s - x_{j_i} & j \in \{2,4\} \\ z_{S_{2_i}} = z_{S_{4_i}} = z_s + R \end{cases} \tag{3.50}$$

54

Where x_{j_i} and R, can be obtained from (3.41) and (3.38) respectively. Substituting calculated values from (3.50) in (3.35) and (3.36), results in magnetic field of the curved wires 2 and 4. Similar to straight wire, for an arbitrary point along z-axis, $(0, 0, z_s)$, due to symmetry, both curved wires will provide same amount of magnetic field in the z direction and cancel each other in x direction, $\vec{B}_{x2_i} = -\vec{B}_{x4_i}$, and consequently, $B_{2_i} = B_{4_i}$. By considering (3.41) and (3.35) :

$$B_{Curve_i} = 2B_{2_i} = \frac{\mu_0 I x_{2_i}}{\pi z_{S_{2_i}} \sqrt{(R + z_{S_{2_i}})^2 + x_{2_i}^2}} \left[-\left(F(k_i) - F(\frac{\pi}{2} - \frac{\varphi_i}{4} | k_i) \right) \right.$$

$$\left. + \left(\frac{R^2 + z_{S_{2_i}}^2 + x_{2_i}^2}{(R - z_{S_{2_i}})^2 + x_{2_i}^2} \right) \left(E(k_i) - E(\frac{\pi}{2} - \frac{\varphi_i}{4} | k_i) \right) \right] \vec{a_z}$$

$$(3.51)$$

where,

$$k_i = \sqrt{\frac{4R z_{S_{2_i}}}{(R + z_{S_{2_i}})^2 + x_{2_i}^2}} \quad . \tag{3.52}$$

In a $N - turn$ structure, total magnetic field density is the summation of B from all the straight and curved wires:

$$(3.47), (3.51) \implies \vec{B}|_{S(0,0,z_s)} = B_{Side} + B_{Curve} = \sum_{i=1}^{N} B_{Side_i} + B_{Curve_i} \ . \tag{3.53}$$

Variable of the sample proposed structure in Fig.3.3, is presented in Table 3.2 which are used to calculate the total magnetic field of the structure.

Total width and length of the structure is calculated by considering table 3.2 and (3.37), :

$$\begin{cases} w = 36.4 \ mm \\ L = 36.4 \ mm \end{cases} \tag{3.54}$$

Table 3.2: Structure parameters

Parameter	Value
Window width (h)	$10\ mm$
Window height (H)	$10\ mm$
Number of turns (N)	15
Wire diameter (d)	$1.76\ mm$
Curve angle (φ)	$30°$ $(\frac{\pi}{6}\ rad)$
Desired point height, z_s	$30\ mm$
Current RMS value (I)	$10\ A$
Frequency	$85\ kHz$

Radius of the structure, width of each turn and curve angle of each turn, can be calculated by substituting (3.54) in (3.38) and (3.40) respectively:

$$\begin{cases} R = 139.04\ mm \\ w_i = 36.4 - (i-1) \times 1.76\ mm \end{cases} \implies \varphi_i = \frac{2w_i}{139.04\ mm} \tag{3.55}$$

By substituting (3.55) in 3.41),(3.44) and (3.50), coordinates of endpoints for each turn is obtained:

$$\begin{cases} |x_{j_i}| = 36.4 - (i-1)1.76 & mm \\ |y_{j_i}| = 139.04\sin(\frac{\varphi_i}{2}) & mm \\ z_{j_i} = 139.04(\cos(\frac{\varphi_i}{2}) - 1) & mm \\ z_{S_{j_i}} = 169.04 & mm \quad for\ j \in \{2,4\} \end{cases} \tag{3.56}$$

Total magnetic field of sample structure can be calculated using the obtained values and superposition method. The magnetic field of each turn is obtained substituting (3.56) in (3.47) and (3.48) to calculate the magnetic field straight wire and is completed by replacing (3.56) in (3.51)-(3.53) to obtain the magnetic field of the curved parts. Total magnetic field density of the sample structure is calculated using superposition method:

$$\vec{B}_{total} = \sum_{i=1}^{15} B_{Side_i} + B_{Curve_i} = 1.16\ mT\ \vec{a}_z\ . \tag{3.57}$$

56

In the next section, conduction loss and FEM calculated magnetic field of the structure is obtained from Ansys Maxwell to verify the analytical results.

3.2.3 FEM Verification

FEM based model of the structure is implemented in Maxwell environment as shown in Fig.3.3. Turns are not designed separately to increase the versatility of the design for optimization purposes. Later, the final optimized structure is modeled in detail to simulate the actual planar structure precisely. Based on FEM calculations, magnetic field density of no core proposed planar structure is presented in Fig.3.11.

(a)

(b)
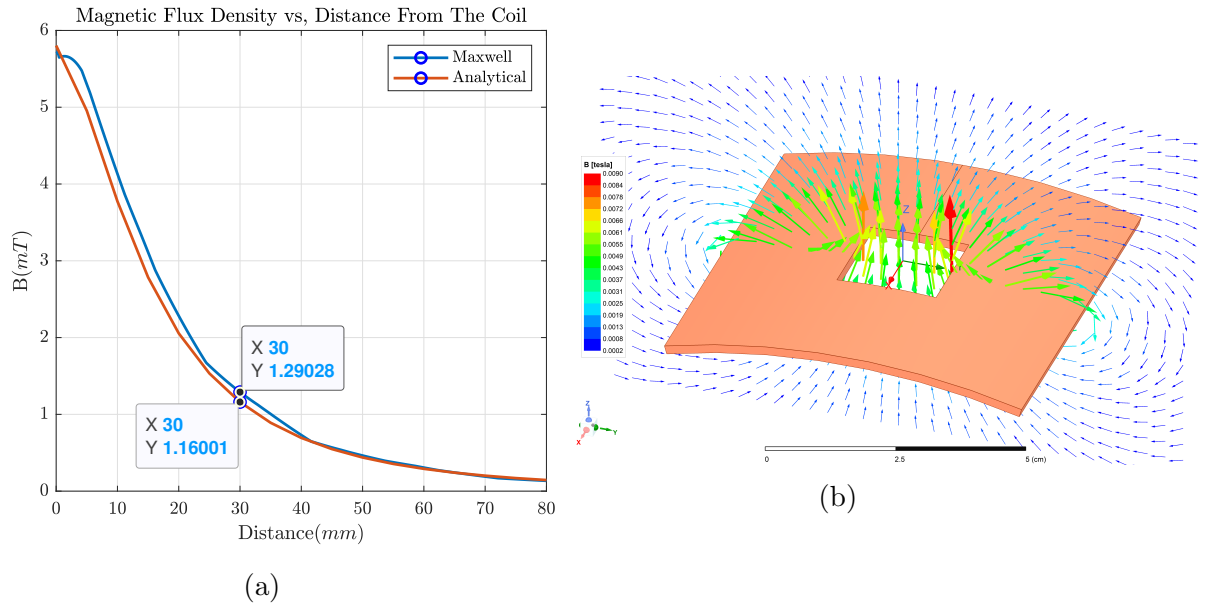
Figure 3.11: Magnetic field of planar no core structure (a) Magnitude with respect to distance (b) Vectors

FEM result will validate the analytical approach with $1.29mT$ at $3cm$ from the coil with applied Lorentz force of $2.6\mu N$. The complete conduction loss is $4W$ including ac losses due to skin and proximity effect which is expected to be higher than the actual loss due to the way of defining the turns. Similar to non-planar structures, core is added to no core structure to improve the magnetic field density consistency outside the coil. Core sticks are used instead of full core to reduce the core loss while

maintaining the benefits of core.

3.3 Planar Structure with Core bars

The effect of core sticks beneath the structure on improving the magnetic field outside the structure is studied in this section. To be able to provide analytical model of the structure with core bars, new mirror method suitable for partial core coverage structure is proposed and then verified by FEM analysis.

Similar to non-planar structure two scenarios are considered: core covering the entire coil area and, core bars beneath the window area. Complete FEM based comparison between both scenarios are provided to show that, between $50 - 70\%$ of core coverage will provide more force to repel the metal particles with low input power.

The analytical model of the structure is needed to obtain the magnetic field at the desired point, S, which is located at $3cm$ from the structure surface.
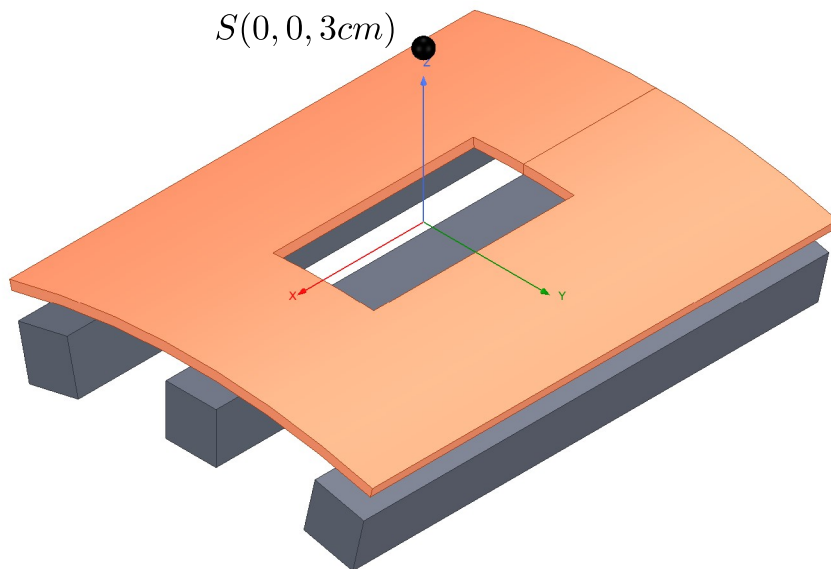
Figure 3.12: Sample bar shaped core structure

3.3.1 Analytical Modeling of Proposed Planar Structure with Core

In this section, novel mirror method is proposed to model the planar structure with partially core coverage. First, analytical model for the planar structure with 100% core coverage is obtained and then, the model is generalized for partially core coverage. According to (2.9) and high relative permeability of $3C94$, the core thickness can be neglected. Although, core curve has the same angle as the coil angle φ, the radius is different. Accordingly, First step is to calculate the core curve radius which is used later for modeling both full and partially core covered structures. According to Fig. 3.13a, core radius of the full core structure, is the same as the radius of circle that contains the core bars in partially covered structure.
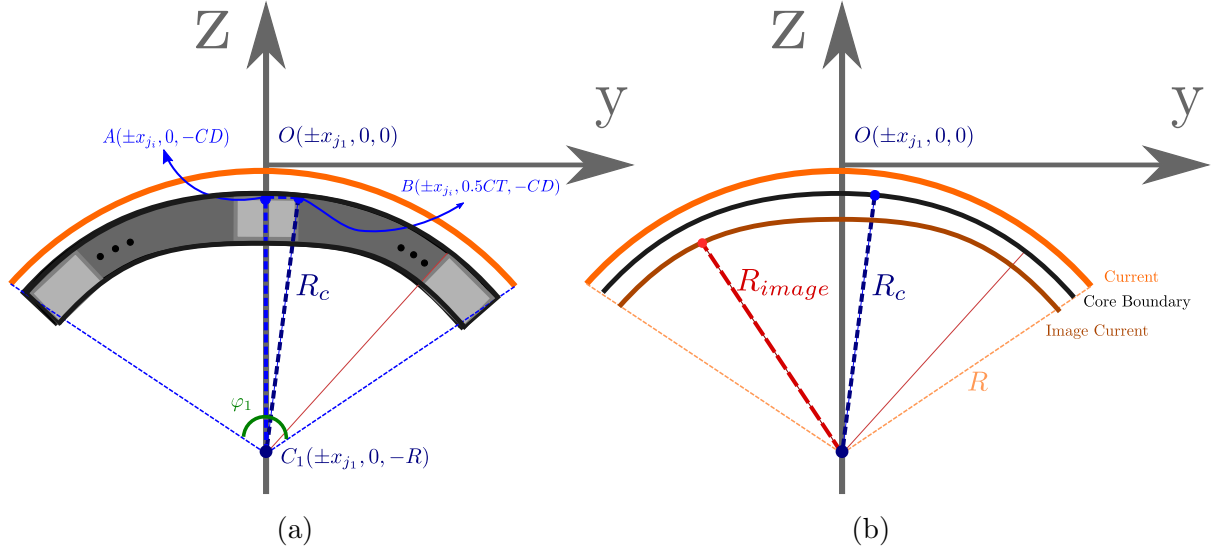
Figure 3.13: Proposed planar structure with core bars (a) Full coverage consist of core bars (b) Image current

In Fig. 3.13, CD is the distance from the core to the origin and CT is core thickness. According to $A\overset{\triangle}{B}C_1$ triangle, the radius of core curve is:

$$\begin{cases} AC_1 = R - CD \\ R_c = \sqrt{AC_1^2 + AB^2} \end{cases} \implies R_c = \sqrt{(R - CD)^2 + (0.5CT)^2} \ . \tag{3.58}$$

Based on the image theory, the image current would have the same curve angle as

the core and actual winding and different radius:

$$R_{img} = R_c - 2 \times (R - R_c) . \tag{3.59}$$

To calculate the magnetic flux density at distance z_s, from the structure, the equivalent distance for the image current is:

$$z_{img} = z_s + 2 \times (R - R_c) . \tag{3.60}$$

Using (3.47), (3.51) and (3.53) the total magnetic flux density of a full core coverage proposed planar structure can be calculated:

$$\vec{B_{Total}} = \vec{B}(0, 0, z_s)|_R + \vec{B}(0, 0, z_{s_{img}})|_{R_{img}} . \tag{3.61}$$
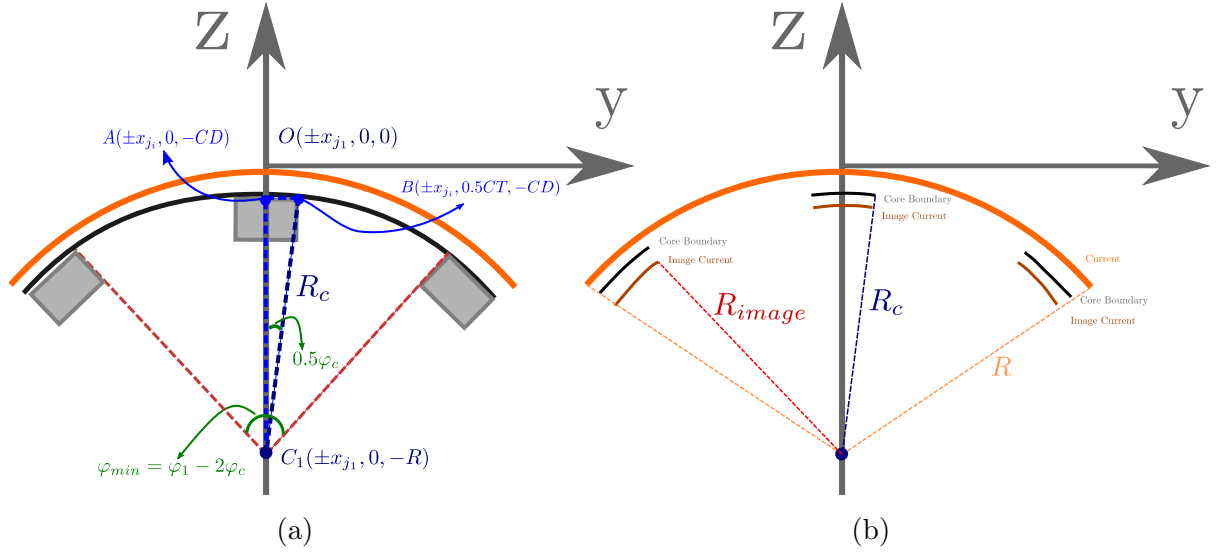
Figure 3.14: Proposed planar structure with core bars (a) Three core bars (b) Related image currents

In three core structure, only parts of the winding which is located above the core will generate image current. As shown in Fig.3.14, side core bars produces image current for turns with carve angles higher than φ_{min}:

$$\varphi_{min} = \varphi_1 - 2\varphi_c, \tag{3.62}$$

60

where φ_c is the equivalent curve angle of a single core bar which can be calculated using (3.58):

$$\varphi_c = 2\arcsin(\frac{0.5 \times CT}{R_c}) \ . \tag{3.63}$$

The three core bars would not cover the turns that have the curve angle lower than φ_{min} and greater than φ_c and accordingly, there is no image current for those turns. As a result, for the side part of the turns, the magnetic flux density caused by image current is:

$$\begin{cases} B_{side_i}|_{z_{s_{img}}, R_{img}} & \varphi_i \in [\varphi_{min}, \ \varphi_1] \cup (0, \ \varphi_c] \\ 0 & Otherwise \end{cases} \tag{3.64}$$

and for the curved part of the turns:

$$\begin{cases} \left(B_{curve_i}(\varphi_i) - B_{curve_i}(\varphi_{min}) + B_{curve_i}(\varphi_c)\right)|_{z_{s_{img}}, R_{img}} & \varphi_i \in [\varphi_{min}, \ \varphi_1] \\ B_{curve_i}(\varphi_i)|_{z_{s_{img}}, R_{img}} & \varphi_i \in (0, \ \varphi_c] \\ 0 & Otherwise \end{cases} \tag{3.65}$$

Although, for the curved part of the turns with curve angle greater than φ_{min}, all three cores would have image current, in the turns with a curve angle lower than φ_c, only the middle core produces image current. Some error is expected for the analytical model of the three core structure specially in higher curve angle as the effect of core's side walls on producing the image current are neglected.

3.3.2 FEM Verification

To evaluate the analytical calculations of the previous section, a structure with 20 turns using a $3.6mm$ wire, $2 \times 10cm^2$ window area and, three $25mm$ core bars is modeled in the Ansys. The curve angle of the structure is changed from $10°$ to $180°$ and the magnetic flux density at $3cm$ from the structure is obtained from Ansys. The magnetic flux density at $3cm$ of the sample proposed structure is calculated based on the derived model for both full core coverage and partially covered structure.

According to analytical and FEM obtained results presented in Fig.3.15, in lower curve angles the three core method would have less error yet as the curve angle increases the three core method error is increased as well and the full core method

would have better accuracy in modeling the structure. As expected, the effect of cores side walls cannot be neglected in higher curve angles.
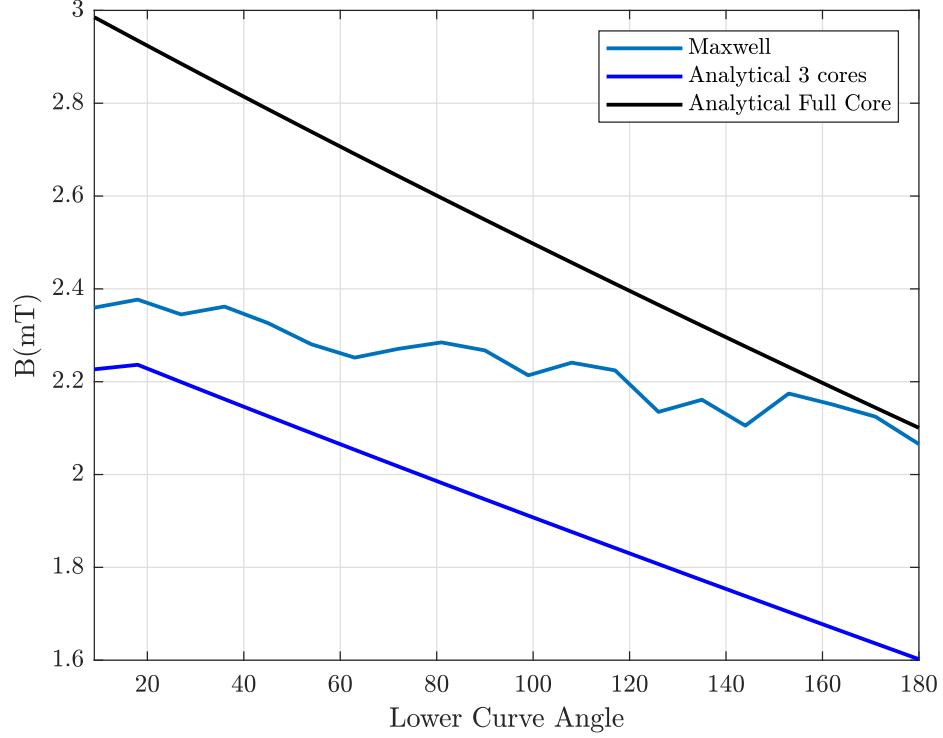
Figure 3.15: Different analytical methods compare to FEM results for a sample winding

To obtain the most accurate analytical model for all curve angles, both models are combined and weighted average of two methods are used. Consequently, new parameter called Core Factor (CF), is introduced to determine the weight of both models in the calculations:

$$CF = \frac{180 - \varphi_1}{180} \tag{3.66}$$

The total magnetic flux density of three core structure can be obtained using the core factor, CF, and calculating the weighted average of both full core and partially covered models:

$$\vec{B}_{total} = \vec{B}_{AirCore} + (1 - CF) \times \vec{B}_{FullCore} + CF \times \vec{B}_{ThreeCore} \ . \tag{3.67}$$

According to Fig.3.16, weighted average model would provide the magnetic flux density with less than 5% for all the curve angles. Using the obtained model on the defined structure at the start of this chapter with $20 \times 20mm$ window area, $16mm$, $3C94$ I cores and 15 turns of $1.76mm$ Litz wire with $10A$, $85kHz$ injected current, the magnetic flux density in $3cm$ from the coil is $1.63mT$.
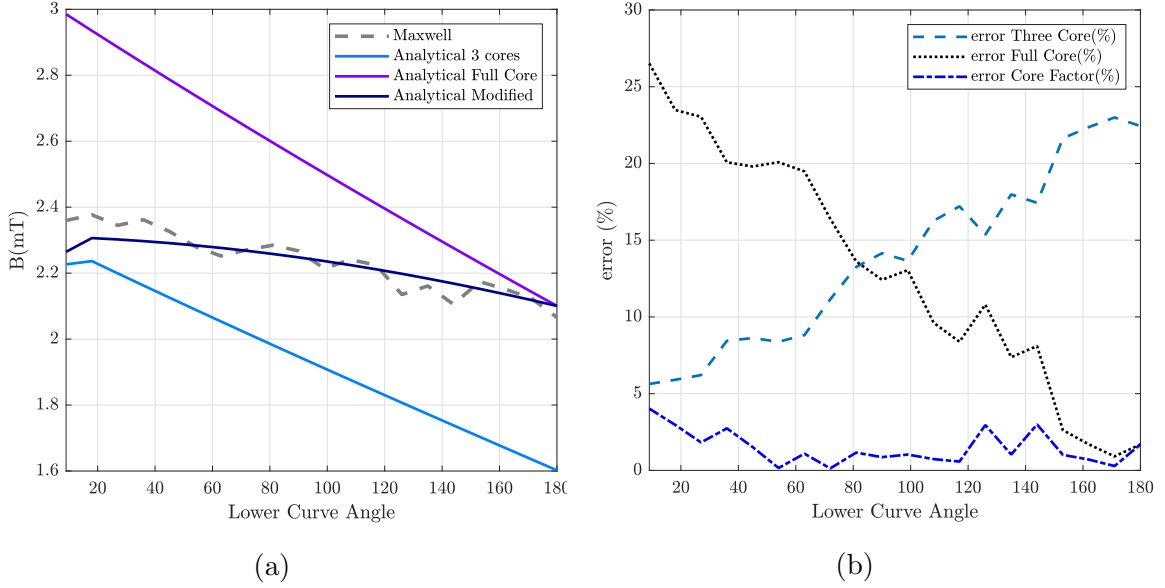
Figure 3.16: Maxwell and Analytical results for the sample structure (a) Magnetic field (b) Calculation error

The FEM analysis is performed on the proposed structure to verified the analytical results. As shown in Fig.3.17, the magnetic flux density at $3cm$ of proposed structure is $1.61mT$ that results in 1.24% computation error. Complete conduction and core losses are $4.2W$ and $3.5mW$ respectively. The applied force is $6.8\mu N$.

Compare to E core structure, magnetic flux density increased 6.637% with the same number of turns, window area and less core material. By structurally optimizing the proposed planar structure, even higher magnetic flux density can be achieved.
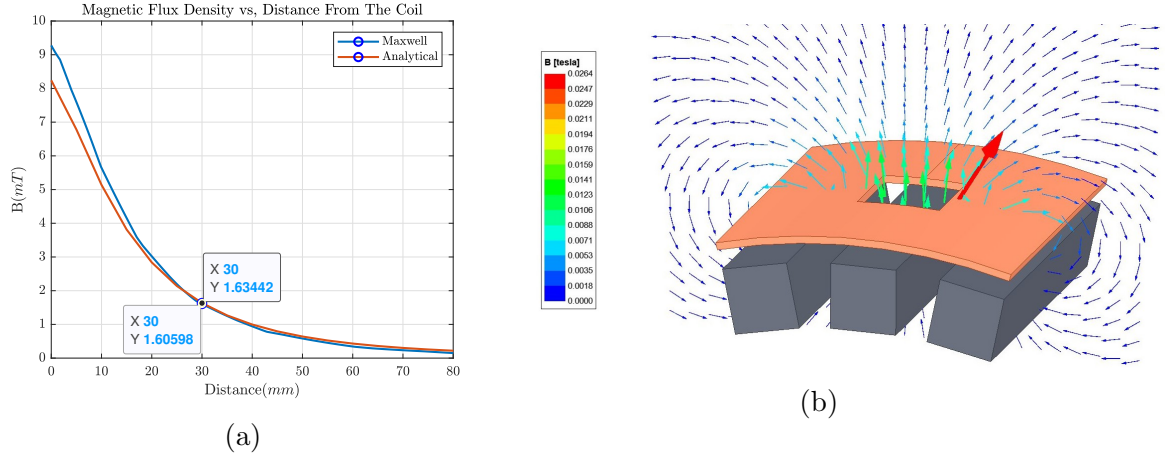
Figure 3.17: Magnetic field of proposed structure (a) Magnitude with respect to distance (b) Vectors

Later it is discussed that the magnetic flux density caused by the planar proposed structure will induce greater force in the metal particles in contrast with E core structure. In the next section, aiming to further increasing of the magnetic field, the complete two winding structure is analyzed in detail.

3.4   Proposed Planar Structure with Resonator Coil

The final proposed planar structure consists of two separate planar structures placed at a distance from each other. The proposed structure, have four design parameters: the window area of the coils, core coverage percent of the coils, distance of the coils and, curve angle of each coil that can be optimized to maximize the magnetic field at the desired distance.

It is possible to design the lower coil such that it has the minimum distance with scrap particles by choosing the curve higher than the drum curve angles to minimize the distance from the particles and maximize the magnetic field at the feeder belt surface.

The simulated structure has 15 turns of $1.76mm$ Litz wire with window area similar to $E80/38/20$ center leg area which is $20 \times 20mm$. The core bars are $16mm$ I bars

and according to working frequency of $85kHz$, the selected material is $3C94$. The distance between the two coils is the same as the E structure with resonator coil which is $8cm$. Curve angles are considered to be $30°$ for the lower coil and $80°$ for the upper coil. The selected values are optimized in the next chapter to maximize the magnitude of the magnetic field at, S, located at $3cm$ from the structure.
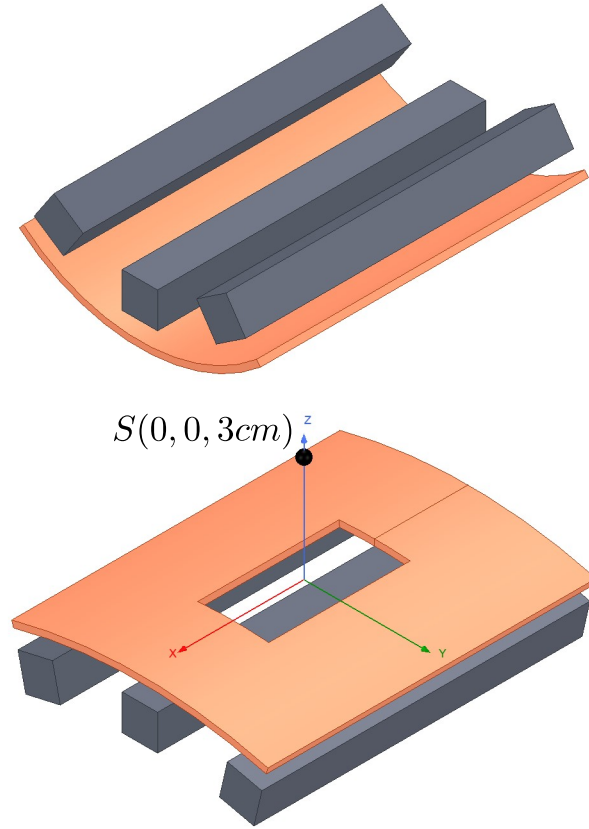
Figure 3.18: Planar structure with resonator coil

3.4.1 Planar Structure with Resonator Coil Modeling and Magnetic Field Calculation

The superposition of both magnetic flux densities from each coil is calculated to obtain the total magnetic flux density. Similar to E core structure with resonator coil, the proposed planar structure with resonator coil can be modeled as planar transformer with a huge air gap using equivalent T-model of Fig. 3.19. According to the circuit model and previous discussions in section 3.19, each coil can have different current

magnitude and phase angle that will affect the total magnitude of flux density of the structure:

$$\vec{B}_{total} = \vec{B}_{Lower}(\varphi_1, z_{down})I_1 \cos(\omega t - \theta_1) - \vec{B}_{Upper}(\varphi_2, z_{up})I_2 \cos(\omega t - \theta_2) \ . \quad (3.68)$$

Unlike E core structure with resonator coil, due to difference in the curve angle of the coils, L_1 and L_2 would not necessary be the same in proposed planar structure with resonator coil. To adjust the magnitude and phase of the secondary winding with respect to the primary current, C_2 and R_L are added to the secondary side of the structure.
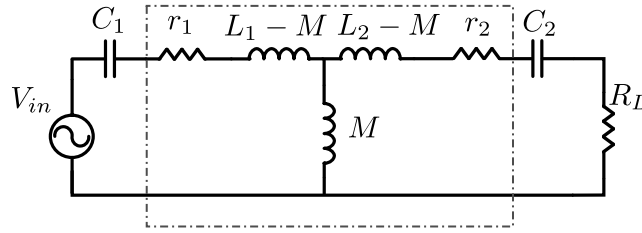
Figure 3.19: planar structure with resonator coil equivalent circuit model

C_1 is used to compensate the self inductance of the primary winding, $L_1 - M$, with same equation as (2.17) in E core structure with resonator coil:

$$C_1 = \frac{1}{(L_1 - M)(2\pi f_{operation})^2} \ . \quad (3.69)$$

Based on (2.18), the magnitude and phase of the secondary current is a function of primary current, C_2 and R_L. As shown in Fig. ?? with proper choice of the circuits design variables, secondary current can be regulated to any arbitrary magnitude and phase with respect to the primary current. According to discussions in the section 2.3, and (3.68), the second coil would have the maximum effect on maintaining the field between the coils with $180°$ phase difference with the primary current.

In the next chapter, the circuit design variables, C_2 and R_L, are used in the optimization process for achieving optimal magnitude and phase for the secondary current. In this section, it is assumed that the currents have the same magnitude of $10A$

as the previous designs with 180° phase difference. The total magnetic flux density using superposition method is:

$$\vec{B}_{total} = \left(\vec{B}_{Lower} \left(\varphi_1, z_{down} \right) + \vec{B}_{Upper} \left(\varphi_2, z_{up} \right) \right) I \cos(\omega t) \ . \qquad (3.70)$$

The distance between the coils is $8cm$ and the magnetic flux density in $3cm$ from the lower coil is desired, as a result:

$$\begin{cases} z_{up} = Distance - z_{down} \\ z_{down} = 3cm \\ Distance = 8cm \end{cases} \implies z_{up} = 5cm \ . \qquad (3.71)$$

The total magnetic flux density of planar structure with resonator coil can be calculated using the proposed mirror method in section 3.3:

$$\vec{B}_{total} = (\vec{B}_{Lower}(30°, 3cm) + \vec{B}_{Upper}(80°, 5cm)) \cos(2\pi t \times 85000) = 2.21mT \ . \quad (3.72)$$

3.4.2 FEM Verification

The analytical result is verified with FEM calculations as shown in Fig. 3.20. The magnetic flux density in $3cm$ from the lower coil from Ansys Maxwell is $2.14mT$ which results in 3.27% error. The complete conduction and core losses are $24.15mW$ and $9.88W$ respectively. The applied force is the highest in the propose planar structure with the resonator coil with the value of $8.4\mu N$.

The planar structure with resonator coil and non-optimized variables has slightly higher magnetic flux density with respect to the largest E core structure. In the next chapter, it is shown that the structurally optimized planar structure will improve the magnetic field significantly. This chapter ends with a multi dimensional comparison between planar and non-planar structures from different aspects including the applied force to the metal scraps.
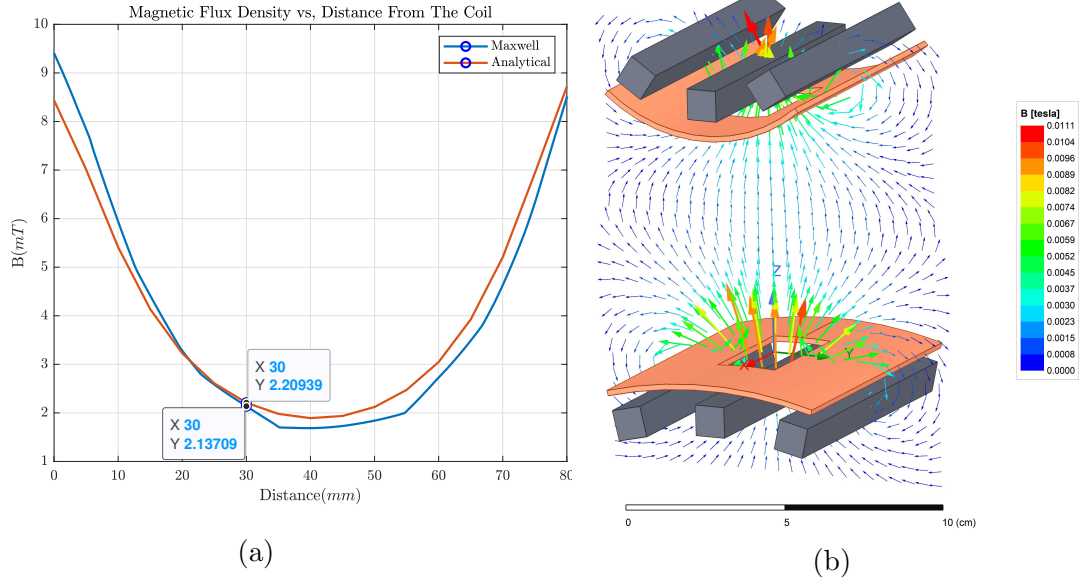
Figure 3.20: Magnetic field of planar structure with resonator coil (a) Magnitude with respect to distance (b) Vectors

3.5 Planar VS. Non-Planar Comparison

In this section, for different constraints, planar and non-planar static separators are analyzed in detail. Six planar and two non-planar structures are used in this comparison with 15 turns of $1.76mm$ Litz wire and working frequency of $85kHz$ and $3C94$ ferrite material. The two non-planar structure are the cases which were analyzed in previous sections large $80/38/20E$ core and small concentrated $30/15/7E$ core.

All planar structures would have $30°$ curve angle with different core sizes and coverage. First one would have three $16mm$ I core bars with $20 \times 20mm^2$ window area same as the large E core main leg area, called $3 - 16B$. Second structure would have $20mm$ I core bars to determine the effect of core size, $3 - 20B$. Third structure would have full $16mm$ thick core coverage with the same window area as the firs two structures, $F - 16B$.

The next three structures would have the window area equal to the area of the smaller non-planar core's main leg area which is $7 \times 7mm^2$ and different cores: one $16mm$ I core, $1 - 16S$, three $16mm$ I core, $3 - 16S$ and, full $16mm$ thickness core

coverage, $F - 16S$, respectively.

There is a $3mm$ copper sphere at $3cm$ from the coils as a reference non-ferrous metal particle to measure the applied Lorentz force. All six structures are modeled in the Ansys Maxwell environment and the results are obtained from the FEM analysis in Ansys. Three tests are performed on the structures and in all tests applied force, provided magnetic field at the reference point, core and conduction losses, injected currents and, input power is obtained from Ansys. In the first test same $1kW$ input power is applied to the coils while In the second test winding are excited to provide $2mT$ magnetic flux density at $3cm$ from the coil. In the final experiment it is investigated that how much power is needed for each coil to induce $9\mu N$ force in the copper sphere.

3.5.1 Equal Input Power

In first experiment, based on the FEM calculated inductance of the structure, the coils are excited with a pre specified voltage to have the equal input power of $1kW$:

$$\begin{cases} P = \dfrac{V^2}{\omega L} \\ \omega = 2\pi \times 85000 \end{cases} \implies V = \sqrt{(1kW)(\omega L_{Ansys})} \ . \tag{3.73}$$

As shown in table 3.3, by injecting same power to the coils, less core material volume of planar structures, leads to lower inductance and accordingly, higher current in same input power test which leads to higher magnetic flux density and induced force. Based on the results, $3 - 20B$ would provide the highest force among all other structures. Although, the $1 - 16S$ structure provides same force, the current magnitude and accordingly losses are higher. According to table 3.3, although the full core structure provides almost the same amount of magnetic flux density, the induced force is 23% less than $3 - 20B$ structure. As a result, in the next experiment it is investigated that how different structures react when they provide same amount of magnetic flux density in the desired point in space.

Table 3.3: Same Input Power Test

Structure	Force (μN)	$B\|_{3cm}$ (mT)	CoreLoss (mW)	Cond.Loss (W)	Current (A)	Power (kW)
80/38/20E	4.46	1.1	294.4	2.06	7.17	1
30/15/7E	0.998	0.4	677.1	4.95	12.45	1
3-16B	7.74	1.8	3.66	4.8	10.62	1
3-20B	9.02	1.84	2.64	4.63	10.41	1
3-16S	8.5	1.7	2.96	5.86	14.07	1
1-16S	9	1.6	3.97	6.2	14.54	1
F-16B	6.94	1.87	2.16	4.6	10.28	1
F-16S	6.96	1.32	2.06	5.78	13.77	1

3.5.2 Equal Magnetic Flux Density

One of the main factors of comparing different structures is to measure the applied force and losses of the structures while providing same amount of magnetic flux density at the specified point in space where the test metal is located at $3cm$ from the coil. Based on the provided results in table 3.4, the input power of planar structures to provide $2mT$ magnetic flux density at $3cm$, is one third of large E structure and 3.5% of small E structure. Power consumption and loss values of planar structure is almost equal although, $1-16S$, $3-16S$ and, $3-20B$ provide higher magnetic flux density with respect to other three planar structures. In the final test, the structures are compared when same amount of force is applied to the copper sphere.

Table 3.4: Same Magnetic Flux Density Test

Structure	Force	B|$_{3cm}$	CoreLoss	Cond.Loss	Current	Power
	(μN)	(mT)	(mW)	(W)	(A)	(kW)
80/38/20E	14.5	**2**	1500	6.72	12.94	3.2
30/15/7E	27.8	**2**	65700	139.03	66	27.8
3-16B	9.7	**2**	4.97	6	11.9	1.25
3-20B	10.6	**2**	3.3	5.45	11.3	1.2
3-16S	11.8	**2**	4.7	8.16	16.6	1.4
1-16S	13.8	**2**	7.1	9.45	18	1.5
F-16B	8.4	**2**	2.82	5.57	11.3	1.2
F-16S	9.2	**2**	3	7.64	15.84	1.3

3.5.3 Equal Force

The ultimate goal of the eddy current separators is to provide high force in the metal particles with the lowest possible power consumption. According to the FEM obtained results in table 3.5, when structures provide the same amount of force on the $3mm$ copper sphere particle located at $3cm$ of the structures surface, planar structures would provide the same amount of force with less input power. The most efficient structure are three core structures with larger window, $3-16B$ following by $3-20B$ with the lowest power consumption and power loss among all other structures.

Table 3.5: Same Applied Force Test

Structure	Force	$B\|_{3cm}$	CoreLoss	Cond.Loss	Current	Power
	(μN)	(mT)	(mW)	(W)	(A)	(kW)
80/38/20E	9	1.58	775.8	4.2	10.2	2.02
30/15/7E	9	1.14	14060	44.9	37.5	9.06
3-16B	9	1.95	4.56	5.6	11.5	1.17
3-20B	9	1.84	2.64	4.63	10.41	1
3-16S	9	1.78	3.26	6.23	14.5	1.07
1-16S	9	1.6	3.97	6.2	14.54	1
F-16B	9	2.13	3.14	5.97	11.7	1.3
F-16S	9	2	3	7.64	15.84	1.3

3.5.4   Conclusion

Based on the performed tests, although not optimized, planar structures provided better force and magnetic flux density with lower input power and accordingly power loss, compared to non-planar E core based structures.

Furthermore, for industrial applications, unlike E core structures, curved planar structure fits in the drum perfectly with minimum distance from the structure's belt surface as shown in Fig.3.21.

It is observed that three core in planar structures, performs better than one core or the full core coverage and accordingly, three core structure with resonator coil is used as the reference structure in the next chapter for the optimization process.
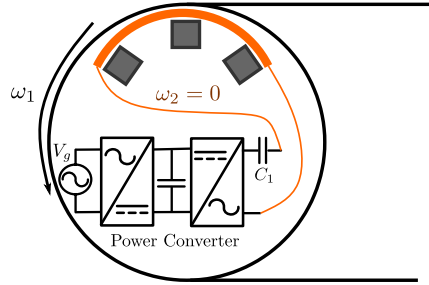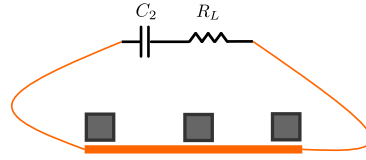
Figure 3.21: Planar Structure with Resonator Coil and Power Electronic Converter

3.6   Summary

In this chapter a novel planar structure consist of concentric spiral turns is introduced. The analytical model of the sample Air core structure with pre-defined design parameters, is derived using the magnetic vector potential formula. The core bars added to structure to improve the consistency of the magnetic field outside the coil. The weighted average of two different modified mirror methods is used to model the proposed planar structure. Second coil added to the structure for further improvement of the magnetic field.

Comprehensive FEM based comparison between planar and non-planar structures is performed which shows the superiority of the proposed planar structure over the non-planar E core based structure in providing better performance with less input power and core losses.

Chapter 4

Proposed Method Optimization and Final Results

The objective of the optimization is to achieve optimal values for design variables of the planar structure with resonator coil aiming to provide the highest possible magnetic flux density at a desired distance, which is considered to be $3cm$ for this research. In this chapter, the complete constrained optimization problem is solved based on a cost function derived for the full scale implementation which then simplified for the lab scaled structure. The analytical and FEM results are verified with experimental results from the scaled down structure.

4.1   Optimization Cost Function Derivation

The total magnetic flux density between two coils can be achieved using the superposition method. The strength of magnetic flux density between two coils is reversely proportional to the distance between the coils, as such lower distances is desirable. However, choosing a low distance between the coils increases the likelihood of the collision of repelled metal particles with the upper coil. Based on simplified calculations and observations, $16cm$ distance is assumed for the coils to benefit from the resonator coil in our studies.

Based on (3.68), the magnitude and phase of the total magnetic flux density depends on the coils current phase and magnitude. For a given parameters, (3.68) can

be rewritten as follows:

$$\vec{B}_{total} = \underbrace{\vec{B}_{Lower}(\varphi_1, z_{down})}_{B_1} I_1 \cos(\omega t - \theta_1) - \underbrace{\vec{B}_{Upper}(\varphi_2, z_{up})}_{B_2} I_2 \cos(\omega t - \theta_2), \quad (4.1)$$

and according to trigonometric identities:

$$\vec{B}_{total} = \underbrace{(B_1 I_1 \cos(\theta_1) - B_2 I_2 \cos(\theta_2))}_{\lambda_1} \sin(\omega t)$$
$$+ \underbrace{(B_2 I_2 \sin(\theta_2) - B_1 I_1 \sin(\theta_1))}_{\lambda_2} \cos(\omega t) \qquad (4.2)$$

Defining new angle ζ as:

$$\zeta = \arctan\left(\frac{\lambda_1}{\lambda_2}\right) \qquad (4.3)$$

and multiplying the numerator and denominator's of (4.2) by $\dfrac{\sqrt{\lambda_1^2 + \lambda_2^2}}{\sqrt{\lambda_1^2 + \lambda_2^2}}$, the magnitude and phase of the total magnetic flux density can be obtained as follows:

$$\vec{B}_{total} = \sqrt{\lambda_1^2 + \lambda_2^2} \left(\sin(\zeta) \sin(\omega t) + \cos(\zeta) \cos(\omega t) \right)$$
$$\qquad (4.4)$$
$$= \sqrt{\lambda_1^2 + \lambda_2^2} \, \cos(\omega t - \zeta)$$

The objective of the optimization cost function is to maximize the magnitude of the total magnetic field or:

$$\sqrt{(B_1 I_1 \cos(\theta_1) - B_2 I_2 \cos(\theta_2))^2 + (B_2 I_2 \sin(\theta_2) - B_1 I_1 \sin(\theta_1))^2} \, . \qquad (4.5)$$

There are two types of optimization variables in the cost function: Mechanical and Electrical. In (4.5), B_1 and B_2 are functions of mechanical variables and I_1 and I_2 are functions of electrical variables.

4.1.1 Optimization Electrical Variables

The equivalent circuit model of the proposed planar structure with resonator coil is presented in Fig. 4.1.
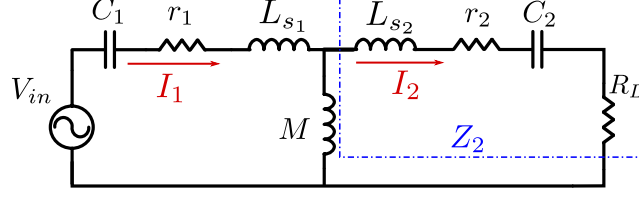
Figure 4.1: Equivalent circuit of proposed planar structure with resonator coil

In section 2.3, it is shown that primary side leakage inductance can be compensated with C_1 and, the secondary current can be regulated with R_L and C_2. Accordingly, the value of L_{s_1} would not affect the optimization process and later, it is obtained from Ansys and compensated with C_1 in the resonance frequency or the working frequency of the structure, which is $85kHz$:

$$C_1 = \frac{1}{L_{s_1}(2\pi f_{operation})^2} \quad .$$

<div align="right">(4.6)</div>

Although the operating frequency does not effect the magnitude of the magnetic flux density, it significantly affects the magnitude of applied force specially in smaller particles [39]. Consequently, frequencies in the range of $85kHz$ leads to acceptable level of forces which can be implemented by conventional power converters.

Because of the large air gap between the coils, the magnetizing inductance is not sensitive to the structure geometry. Based on the prior studies in the previous chapters, the magnetizing inductance value is selected at $15\mu H$ which is the same for different proposed planar structures in the optimization.

In the design, R_L is selected to set the secondary side current at a desired value. The self inductance value of the secondary coil, L_{s_2}, which is dependent on the structure geometry, cannot be used in the optimization cost function directly. Accordingly, secondary phase angle θ_2 is preferred as an optimization variable instead of geometry related leakage inductance or secondary capacitor, C_2, value. Based on Fig.4.1, it is assumed that r_1 and r_2 have negligible values and V_{in} is the phase reference. The **lagging** phase angle of the secondary or θ_2, is the angle of Z_2 impedance and by

assuming the use of compensation capacitor, C_1:

$$\angle Z_2 = \arctan\left(\frac{\omega^2 L_{s_2} C_2 - 1}{R_L \omega C_2}\right) = \theta_2 \tag{4.7}$$

and the **lagging** phase angle of the primary current which is the angle of equivalent total impedance with respect to the primary side in the circuit is:

$$Z_{total} = Z_2 \parallel M \implies \angle Z_{total} = \frac{\pi}{2} + \theta_2 - \arctan\left(\frac{\omega^2 C_2 (M + L_{s_2}) - 1}{R_L \omega C_2}\right) \tag{4.8}$$

and by replacing (4.7) in (4.8):

$$\angle Z_{total} = \frac{\pi}{2} + \theta_2 - \arctan\left(\tan(\theta_2) + \frac{\omega M}{R_L}\right) = \theta_1 \ . \tag{4.9}$$

Based on (4.9), θ_1 can be expressed as other optimization variables R_L and θ_2. According to the equivalent circuit model in Fig. 4.1:

$$|I_2| = \frac{Z_{total}}{Z_2} |I_1| = \frac{\omega^2 M C_2}{\sqrt{(R_L \omega C_2)^2 + (\omega^2 C_2 (L_{s_2} + M) - 1)^2}} |I1| \tag{4.10}$$

and by including (4.7) in (4.10):

$$|I_2| = \frac{\omega M}{R_L \sqrt{1 + \left(\tan(\theta_2) + \frac{\omega M}{R_L}\right)^2}} |I_1| \ . \tag{4.11}$$

At this point, θ_2, R_L, and I_1 are electrical variables of the optimization and all other parameters can be expressed using those design parameters. The value of V_{in} is needed as well to calculate the input power of the structure which can be obtained based on the equivalent circuit:

$$V_{in} = |Z_{total}||I_1| = \frac{R_L \omega M \sqrt{1 + \tan(\theta_2)^2}}{\sqrt{R_L^2 + (R_L \tan(\theta_2) + \omega M)^2}} |I_1| \ . \tag{4.12}$$

The only unknown variable is C_2 which is determined at the end of optimization process based on the leakage inductance values according to (4.7).

Consequently, electrical parameters and their feasibility region are:

$$Electrical\ Variables: \begin{cases} \theta_2 & \in \left[\frac{-\pi}{2}, \frac{\pi}{2}\right] \\ \\ R_L & \in [0,\ 100] \\ \\ I_1 & \in [1,\ 20] \end{cases} \tag{4.13}$$

4.1.2 Optimization Mechanical Variables

The mechanical variables are shown in Fig.4.2. The first optimization variables are curve angles of the lower and upper structures, φ_1, and φ_2 and the number of turns, N which is considered to be the same for both coils. Window area width, $2h$, is the effective width of the separator and as the window area width becomes wider the magnitude of flux in the middle becomes smaller, at the same time as the window area becomes narrower, the working width of the structure becomes smaller. Consequently, between $1 - 4cm$ is a proper choice for h which is the half of effective width as shown in Fig.4.2.
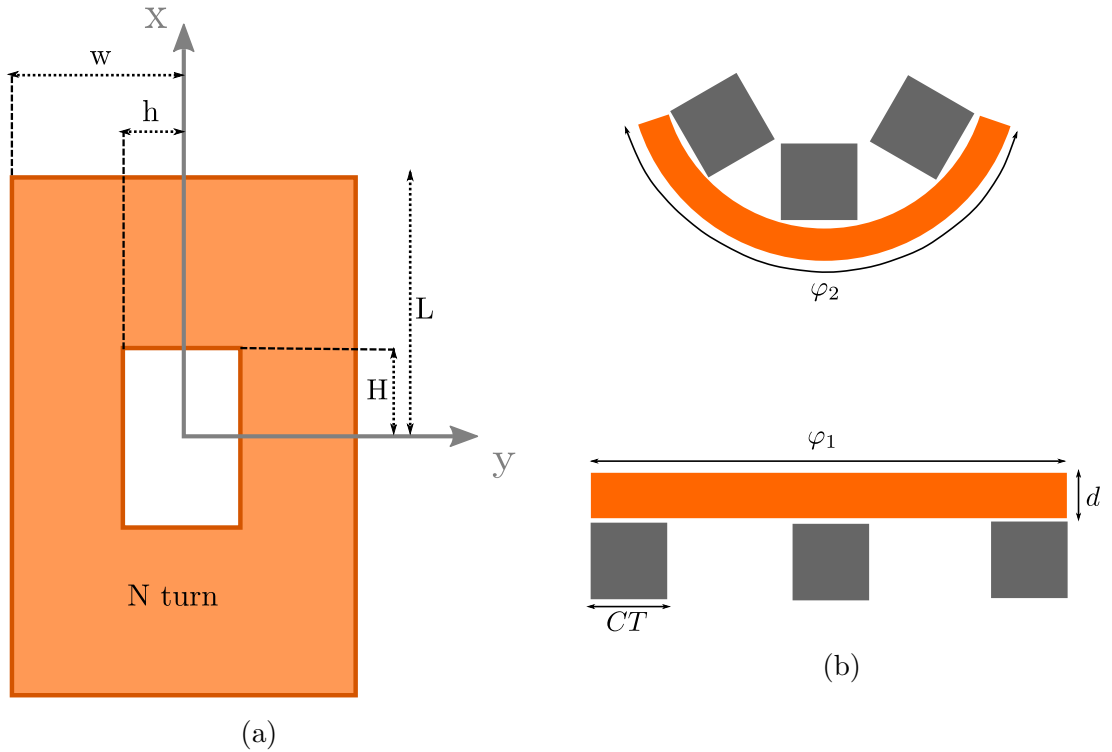
Figure 4.2: Proposed planar structure with the resonator coil optimization parameters (a) Top view in flat state (b) side view

The working length of the separator, $2H$, is selected to be at least $60cm$ to be comparable with the existing industrial magnetic drums. Last mechanical variable is coverage percentage of the core bars, σ. Based on the analytical method explained in the previous chapter, it is assumed that cores are uniformly distributed in the middle

and far ends of the structure to use the three core method explained in section 3.3 in the calculations. Core thickness, CT is needed to use the weighted average mirror method which can be calculated as follows:

$$CT = \frac{2w}{3}\sigma \ .$$

(4.14)

where, $w = h + N \times d$ is half of the width of the flat structure as shown in Fig.4.2. In summary, the aforementioned mechanical parameters and the feasibility ranges are listed as follows:

$$Mechanical\ Variables: \begin{cases} \varphi_1 & \in [0, 180] \\ \varphi_2 & \in [0, 180] \\ N & \in \mathcal{N} \\ h & \in [1, 4] \\ H & \in [30cm, 75cm] \\ \sigma & \in [0, 100] \end{cases} .$$

(4.15)

The usable space is inside the drum and accordingly size of the structure which is related to window area and the wire size is important as well. Although, Litz wire with lower equivalent AWG size, is able to pass higher current, the number of turns is limited to fit the structure in the drum. On the other hand, in thinner wires the current is lower but the number of turns can be much higher. Consequently, wire diameter, d, is another optimization variable.

The skin effect is ignored in the optimization and later, proper Litz wire with equivalent AWG size is selected according to the operating frequency.

The current magnitude is related to wire size and current density, J, and by selecting wire diameter as a design variable, the current magnitude should be calculated using the wire diameter, d, current density, J and, filling factor, k_w as follows:

$$|I_1| = k_w J d$$

(4.16)

Assuming maximum allowable current density, J, for the copper wires which is $5 \times 10^6 \frac{A}{m^2}$ and, filling factor of 60%, (4.16) is simplified to:

$$|I_1| = 3 \times 10^6 \ d$$

(4.17)

Instead of the primary current magnitude $|I_1|$, (4.17) is used in the optimization process and d is the last optimization variable.

4.1.3 Cost Function in terms of Optimization Variables

The optimization cost function is formed based on nine design variables including the six mechanical and three electrical parameters. Mechanical variables are used to calculate B_1 and B_2 in (4.1) and using wire diameter, d, and (4.17), the magnitude of the primary current is obtained. The remaining variables, R_L, and θ_2 ware used to obtain the magnitude of the secondary current and lagging phase angle of the primary current. After calculating both currents phase and magnitude, total magnetic flux density at desired distance which is $3cm$ of the structure surface are obtained from (4.5):

$$\sqrt{\left(B_1 I_1 \cos\left(\theta_1\right) - B_2 I_2 \cos\left(\theta_2\right)\right)^2 + \left(B_2 I_2 \sin\left(\theta_2\right) - B_1 I_1 \sin\left(\theta_1\right)\right)^2} , \quad (4.18)$$

In which:

$$\theta_1 = \frac{\pi}{2} + \theta_2 - \arctan\left(\tan\left(\theta_2\right) + \frac{\omega M}{R_L}\right) \quad (4.19)$$

and:

$$|I_1| = 3 \times 10^6 \ d,$$

$$|I_2| = \frac{3 \times 10^6 \ d\omega M}{R_L\sqrt{1 + \left(\tan\left(\theta_2\right) + \dfrac{\omega M}{R_L}\right)^2}} . \quad (4.20)$$

Also, B_1 and B_2 can be obtained from:

$$B = B_{AirCore} + (1 - CF) \times B_{FullCore} + CF \times B_{ThreeCore} , \quad (4.21)$$

where $B_{FullCore}$ and $B_{ThreeCore}$ are explained in section 3.3.1 and CF is:

$$CF = \frac{180 - \varphi}{180} . \quad (4.22)$$

$B_{AirCore}$ can be obtained from:

$$B_{AirCore} = \sum_{i=1}^{N} B_{Side_i} + B_{Curve_i} \, . \tag{4.23}$$

in which:

$$B_{Side_i} = \frac{\mu_0 I}{2\pi\alpha_i^2} \left(\frac{x_{1_i} y_{1_i}}{\sqrt{x_{1_i}^2 + \alpha_i^2}} \right) \vec{a_z} \, , \tag{4.24}$$

in which:

$$\alpha_i = \sqrt{y_{1_i}^2 + (z_s - z_{1_i})^2)} \tag{4.25}$$

and,

$$\begin{cases} x_{1_i} = -(L - (i-1)d) \\ \\ y_{1_i} = R\sin(\frac{\varphi_i}{2}) \\ \\ z_{1_i} = R(\cos(\frac{\varphi_i}{2} - 1)) \end{cases} \tag{4.26}$$

In which, $R = \dfrac{2(h + N \times d)}{\varphi} = \dfrac{2w}{\varphi}$ and, $\varphi_i = \dfrac{2(w - (i-1)d)}{R}$. Accordingly:

$$B_{Curve_i} = = \frac{\mu_0 I x_{2_i}}{\pi z_{S_{2_i}} \sqrt{(R + z_{S_{2_i}})^2 + x_{2_i}^2}} \left[-\left(F(k_i) - F(\frac{\pi}{2} - \frac{\varphi_i}{4}|k_i) \right) \right.$$

$$\left. + \left(\frac{R^2 + z_{S_{2_i}}^2 + x_{2_i}^2}{(R - z_{S_{2_i}})^2 + x_{2_i}^2} \right) \left(E(k_i) - E(\frac{\pi}{2} - \frac{\varphi_i}{4}|k_i) \right) \right] \vec{a_z} \tag{4.27}$$

where,

$$k_i = \sqrt{\frac{4R z_{S_{2_i}}}{(R + z_{S_{2_i}})^2 + x_{2_i}^2}} \tag{4.28}$$

4.2 Optimization Constraints

The first constraint is the lower coil curve angle to be more than a specific angle aiming to achieve the minimum distance with the feeder belt. According to Fig.4.3, in the optimization process, for each set of the variables, if the curve angle of the

lower structure is smaller than equivalent drums angle, φ_{drum}, the structure would not fit perfectly inside the roller.

(a)   (b)   (c)
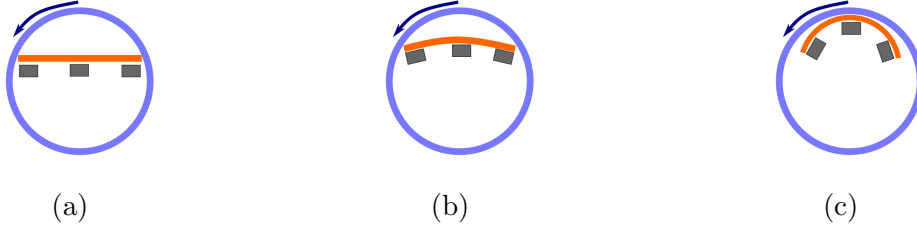
Figure 4.3: Distance of the lower structure from surface belt in (a) flat, (b) partially, and (c) fully curved structure

The minimum curve angle, φ_{drum}, can be calculated using drum diameter, R_{drum}, which is a known variable as follows:

$$w = h + N \times d \implies \varphi_{drum} = \frac{2w}{R_{drum}} \implies \varphi_1 \geq \frac{2(h + N \times d)}{R_{drum}} \ . \tag{4.29}$$

Curve angle of the lower coil should be greater than φ_{drum}, in (4.29) for a perfect fit. The other geometry related constraint is the total width of the structure which should be less than drum's diameter.
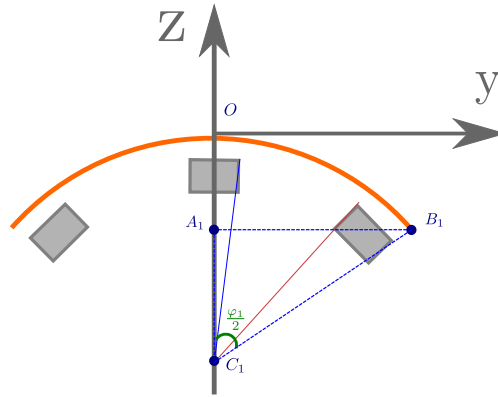
Figure 4.4: Side view of the curved structure

Based on Fig.4.4, structure width in the curve state is $2 \times A_1B_1$ which can be

calculated as follows using $A_1 \overset{\triangle}{B_1} C_1$ right triangle:

$$\begin{cases} A_1 B_1 = R\sin(\frac{\varphi_1}{2}) \\[2mm] R = \dfrac{2w}{\varphi_1} \\[2mm] w = h + N \times d \end{cases} \implies \frac{(h + N \times d)}{\varphi_1}\sin(\frac{\varphi_1}{2}) \le R_{drum} \ . \qquad (4.30)$$

In the following equation w is the half of total width of the structure in flat state. Industrial feeders drum diameter, $2R_{drum}$, has a range of $70 - 150cm$ with the length of around $200cm$. Accordingly, total length of the structure, $2L$, should be less than feeder length, FL:

$$L = H + N \times d \implies 2 \times (H + N \times d) \le FL \qquad (4.31)$$

Next constraint is on the input power of the proposed static planar structure. To achieve better performance comparison, the maximum possible input power of the proposed structure is considered to be equal to the input power of the motor that is used to rotate the magnetic drums in the existing industrial eddy current separator products which is in the range of $P_{motor} = 7 - 11kW$ [21]. Later, it is shown that power consumption of the proposed structure is significantly lower than conventional separators. The input power can be calculated using the RMS values of input current and voltage:

$$P_{in} = |V_{in}||I_1|\cos(\theta_1) \le P_{motor} \qquad (4.32)$$

By replacing $|I_1|$ with $k_w Jd = 3 \times 10^6 \ d$ and substituting $|V_{in}|$ and θ_1 with (4.12) and (4.9), the input power of the proposed structure is:

$$\left| \left(\frac{-\omega M \, (k_w Jd)^2 \, \sqrt{1 + \tan{(\theta_2)}^2}}{\sqrt{1 + \left(\tan{(\theta_2)} + \frac{\omega M}{R_L}\right)^2}} \right) \sin\left(\theta_2 - \arctan\left(\tan{(\theta_2)} + \frac{\omega M}{R_L}\right)\right) \right| \le P_{motor}$$

$$(4.33)$$

To limit temperature rise, the current density, J, of the secondary side should not exceed the acceptable value of $5 \times 10^6 \frac{A}{m^2}$. Assuming the filling factor of 0.6, which is

the same as the primary side:

$$\begin{cases} |I_1| = 3 \times 10^6 \ d \\ |I_2| = |Z_{total}||I_1| \\ |I_2| \leq 3 \times 10^6 \ d \end{cases} \tag{4.34}$$

and by considering (4.11), (4.34) results in:

$$\frac{|I_2|}{|I_1|} = \frac{\omega M}{R_L \sqrt{1 + \left(\tan(\theta_2) + \dfrac{\omega M}{R_L}\right)^2}} \leq 1 \tag{4.35}$$

The complete optimization cost function is achieved by defining all constraints in (4.29)-(4.35). The objective function is to maximize the magnitude of the magnetic flux density at $3cm$ from the lower coil and, $13cm$ from the upper coil using (4.4):

$$\vec{B}_{total} = \sqrt{\lambda_1^2 + \lambda_2^2} \ \cos(\omega t - \zeta) \tag{4.36}$$

where $\zeta = \arctan(\dfrac{\lambda_1}{\lambda_2})$, and λ_1, λ_2 are:

$$\begin{cases} \lambda_1 = B_1 I_1 \cos(\theta_1) - B_2 I_2 \cos(\theta_2) \\ \lambda_2 = B_2 I_2 \sin(\theta_2) - B_1 I_1 \sin(\theta_1) \end{cases}. \tag{4.37}$$

The optimization cost function along with the constraints are solved to achieve the design parameters of the industrial sized drums. Implementing an industrial sized separator is challenging in the lab accordingly, design variables of a 90% scaled down prototype with relaxed constraints are obtained in the next section to implement and verify the analytical and FEM obtained results in this dissertation.

4.3   Scaled Down Prototype

In his section, the relaxed optimization cost function for achieving the optimized scaled down proposed structure is derived by introducing relaxed optimization variables. Later, the optimization cost function is solved in the Global Optimization Toolbox of the Matlab software using the **fmincon** solver which is used for non linear optimization problems with non linear constraints.

According to the design variables of the optimized structure, all the structure parameters are achieved at the end of this section to be used later in producing the prototype.

4.3.1 Scaled Down Optimization Variables

In this section the optimization variables of the scaled down prototype is introduced. Due to limited wire inventory of the Lab, $413 \times AWG36$, Litz wire with current rating of $20A$ is used for the scaled down prototype. The optimized structure is used for verification of the analytical and FEM modeling and accordingly, there is no non-ferrous metal separation in the prototype and the window area is limited to a $2 \times 4 \ cm^2$ rectangle to have the maximum possible number of turns.

The structure is printed with the Fortus 450mc 3D printer [40] and according to the tray size of the printer and the selected wire diameter which is $3.5mm$, the maximum number of turns, N, which is 20, is selected.

Based on market availability, $100/25 \ I$ core bars [41] with $3C94$ material is used and accordingly, using core thickness, CT whis is $25mm$ for the selected core and width of the structure, $2W$, from (3.37),the core coverage percentage, σ is:

$$\sigma = 100 \times \frac{3CT}{2w} = 100 \times \frac{3 \times 25}{2 \times (10 + 20 \times 3.6)} = 45.73\% \quad . \tag{4.38}$$

Consequently, among the mechanical variables, Four are fixed in the prototype including: window width, working length, number of turns and core coverage percentage. The other two mechanical variables which are both coils curve angles are used in the optimization. In the electrical variables, due to pre selecting the wire size, instead of wire diameter, the actual value of the primary current is used in the optimization. The other two variables, R_L and θ_2 will remain unchanged. List of complete scaled

down design variables are:

$$\begin{cases} \varphi_1 & \in [0, 180] \\ \varphi_2 & \in [0, 180] \\ I_1 & \in (0, 20] \\ \theta_2 & \in [\frac{-\pi}{2}, \frac{\pi}{2}] \\ R_L & \in [0.06, 100] \end{cases} \quad . \tag{4.39}$$

After introducing the design parameters of the scaled down prototype, the relaxed constraints are introduced in the next section.

4.3.2 Scaled Down Constraints

There is no drum for the prototype and consequently there is no limitation for the lower coil angle. Also, the structure length is constant with pre specified window area, number of turns and, wire diameter and accordingly, the first constraint is on the input power. The California Instrument $AST3003$ ac source [42] is used as the power source of the structure. According to $AST3003$ datasheet, the ac source can provide maximum power of $3kW$ which is the input power limit of the structure. The maximum frequency of $AST3003$ ac source is $4kHz$ which is selected as the working frequency of the scaled down structure. According to (4.33):

$$\left| \left(\frac{-I_1^2 \omega M \sqrt{1 + \tan(\theta_2)^2}}{\sqrt{1 + \left(\tan(\theta_2) + \frac{\omega M}{R_L} \right)^2}} \right) \sin \left(\theta_2 - \arctan \left(\tan(\theta_2) + \frac{\omega M}{R_L} \right) \right) \right| \le 3kW \tag{4.40}$$

Second constraint would be limiting the magnitude of the secondary current which cannot exceed $20A$:

$$\begin{cases} |I_2| = |Z_{total}||I_1| \\ |I_2| \le 20 \end{cases} \quad \overset{(4.11)}{\Longrightarrow} \quad \frac{\omega M}{R_L \sqrt{1 + \left(\tan(\theta_2) + \frac{\omega M}{R_L} \right)^2}} |I_1| \le 20 \ . \tag{4.41}$$

The last constraint is on the input voltage which is the voltage of the ac source. The $AST3003$ ac source maximum voltage in single phase mode is $400V$ and accordingly,

the structure input voltage, V_{in}, should be less than $400V$:

$$(4.12) \implies \left(\frac{\omega M \sqrt{1 + \tan{(\theta_2)}^2}}{\sqrt{1 + \left(\tan{(\theta_2)} + \frac{\omega M}{R_L} \right)^2}} \right) |I_1| \leq 400 \qquad (4.42)$$

In the last section of this chapter, the optimization cost function is solved in the Matlab to achieved the optimized design variables and magnetic field of the optimized structure.

4.3.3 Scaled Down Optimization

Matlab non-linear optimization toolbox is used for optimizing the magnetic flux density problem. First step would be defining the vector of variables. The scaled down variables are: lower and upper curve angles, primary side current, lagging degree of the secondary current and, added resistor at the secondary side, R_L:

$$x = [\varphi_1, \varphi_2, I_2, \theta_2, R_L] . \qquad (4.43)$$

The feasibility region of the parameters are:

$$\begin{cases} x_{min} = [0, 0, 1, -90, 0.06] \\ \\ x_{max} = [180, 180, 20, 90, 100] \end{cases} . \qquad (4.44)$$

The objective is to maximize $\sqrt{\lambda_1^2 + \lambda_2^2}$ or similarly, to minimize $-\sqrt{\lambda_1^2 + \lambda_2^2}$ in (4.4). The complete form of the optimization cost function is:

$$\min_{\varphi_1, \varphi_2, I_2, \theta_2, R_L} \quad -\sqrt{\lambda_1^2 + \lambda_2^2}$$
$$\text{s.t.} \quad P_{in} \leq 3000$$
$$I_2 \leq 20 \qquad (4.45)$$
$$V_{in} \leq 400$$

where:

$$\begin{cases} \lambda_1 = B_1 I_1 \cos{(\theta_1)} - B_2 I_2 \cos{(\theta_2)} \\ \lambda_2 = B_2 I_2 \sin{(\theta_2)} - B_1 I_1 \sin{(\theta_1)} \end{cases} . \qquad (4.46)$$

There are different optimization algorithms in the Matlab non-linear optimization toolbox. The global search algorithm with **fmincon** solver which is used for minimizing optimization problems with non-linear constraints would have the best results among the other methods. After running the optimization in the Matlab, the optimized feasible points are achieved:

$$x_{opt.} = [101.7, 0, 20, -85.87, 0.06] .\tag{4.47}$$

According to the optimization results, flat upper coil would act better in maintaining te field between the coils. According to achieved load resistor which is $60m\Omega$, the winding self resistor is enough and there is no need to add extra resistors to the secondary side of the circuit . The lagging degree of the secondary side is $-85.87°$ and according to (4.9) the lagging degree of the primary side is:

$$\theta_1 = \left(\frac{\pi}{2} + \theta_2 - \arctan\left(\tan(\theta_2) + \frac{\omega M}{R_L}\right)\right) \times \frac{180}{\pi} = 86.39° .\tag{4.48}$$

As expected the phase difference between the currents is almost $180°$ to get the most from the resonator coil. Current magnitude of the secondary coil and structure input voltage can be obtained from (4.11) and (4.12) respectively:

$$\begin{cases} I_2 = \dfrac{\omega M}{R_L\sqrt{1 + \left(\tan(\theta_2) + \frac{\omega M}{R_L}\right)^2}} \, |I_1| = 17.48 \ A \\[20pt] V_{in} = \dfrac{\omega M\sqrt{1 + \tan(\theta_2)^2}}{\sqrt{1 + \left(\tan(\theta_2) + \frac{\omega M}{R_L}\right)^2}} = 14.58 \ V \end{cases}\tag{4.49}$$

The input power obtained from (4.40), is less than $300W$. The RMS value of total magnetic flux density at $3cm$ from the lower coil calculated using (4.4) is, $5.36mT$. In the next chapter, the FEM analysis is performed on the optimized structure and the structure is implemented to obtain the inductance matrix and verify the analytical and Ansys FEM results.

4.4 Summary

This chapter discusses the effort of deriving an optimization cost function to maximize the magnetic field at a specific point between the coils of the proposed structure. First, optimization parameters of the industrial sized structure is introduced and based on the limitations, the constraints of the optimization cost function is achieved. The optimization problem is then redefined with relaxed constraints to achieve the specification of a 90% scaled down prototype. At the end of this chapter, the optimized variables of the scaled down prototype is achieved by solving the relaxed cost function using the non-linear optimization toolbox of Matlab.

Chapter 5

Experimental Results

In this chapter the optimized structure is implemented to verify the analytical and FEM based calculations with the measured magnetic field from the structure.

To improve the accuracy, the optimized structure is implemented with industrial 3D printers at the University of Alberta. After obtaining the parameters of the proposed structure, a special case for the turns of the optimized structure is designed in the solidworks. The case is printed on Stratasys Fortus 450mc industrial printer [40] located at the Elko engineering garage facility [43] at the university of Alberta. Based on availability, acrylonitrile styrene acrylateor, ASA, [44] material is used for the printer which provides proper mechanical and thermal characteristics for the proposed structure.

5.1   Experiment Setup

The special case for the winding is designed in the SolidWorks. The thickness of the walls between turns of the spiral winding is $1mm$ which is the thinnest wall that Fortus 450mc printer can print. The 3D model of the structure designed in SolidWorks is presented in Fig.5.1.

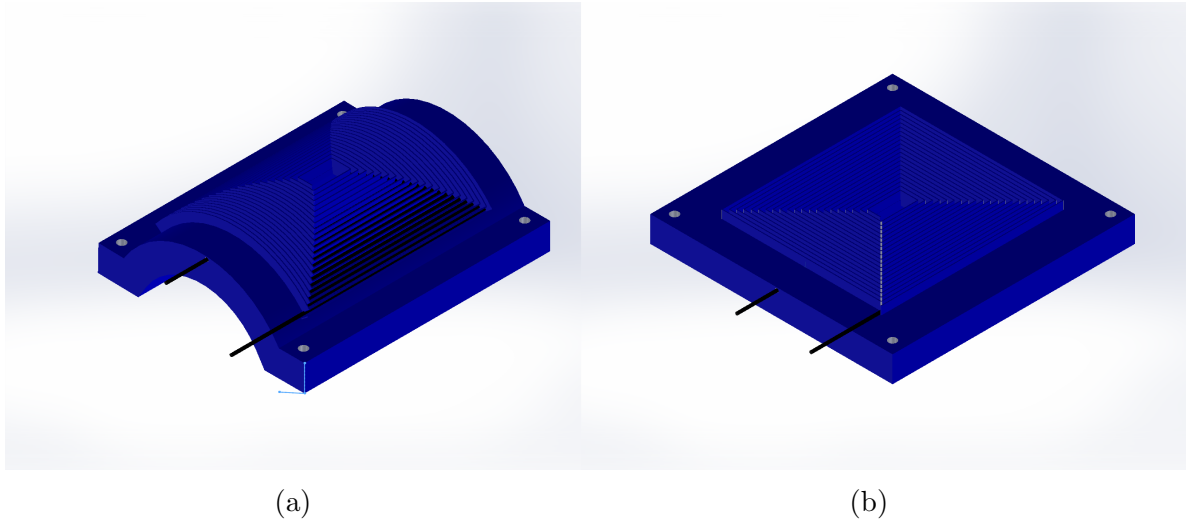|	
(a)	(b)

Figure 5.1: 3D model of the designed case for the coils a) The lower coil and b) The upper coil

The designed model is sent to 3D printer with acrylonitrile styrene acrylate, also known as ASA as the printing material. Distance of the coils in scaled down prototype is $8cm$ and accordingly, special legs are designed in the solidworks and then 3D printed to maintain the distance between the coils. The complete optimized proposed planar structure is presented in Fig.5.2.
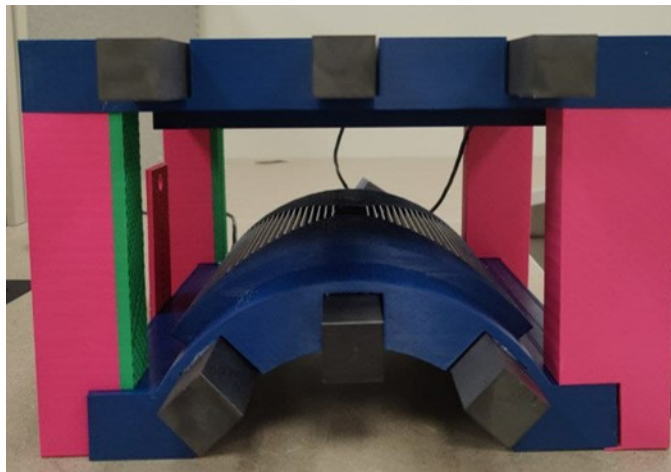

Figure 5.2: Implemented structure printed with Fortus 450mc printer and ASA material

5.1.1 Parameter Extraction

The detailed model of the optimized proposed planar structure, in the Ansys Maxwell is presented in Fig.5.3.
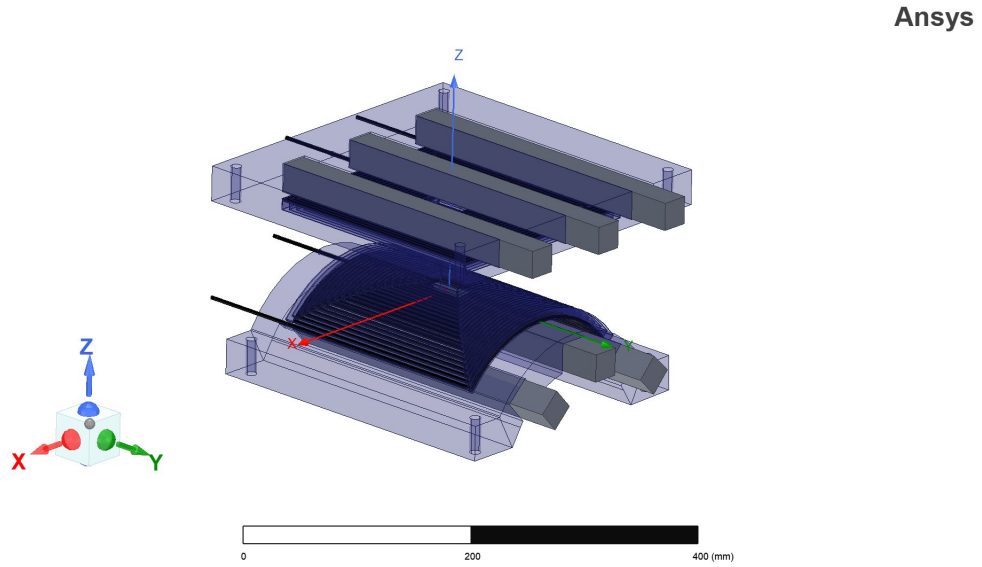

Figure 5.3: Model of the structure in the Ansys Maxwell

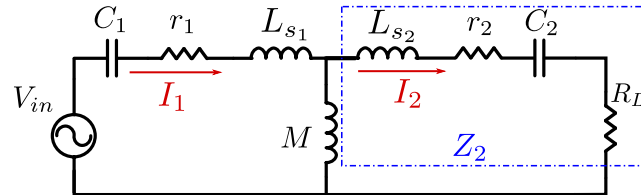The FEM analysis is performed on the Ansys model to obtain the inductance values presented in Fig. 5.4.

Figure 5.4: Equivalent circuit of proposed planar structure with resonator coil

The actual inductance values from the structure is measured to verify the FEM values as listed in table 5.1.

Table 5.1: Inductance values

Inductance	Structure	Maxwell
$\mathbf{L_{lower}}$	51.29 μH	52.88 μH
$\mathbf{M}$	15.52 μH	15.58 μH
$\mathbf{L_{upper}}$	46.69 μH	48.87 μH

The Ansys values matches the measured values from the structure and one can see that the measured magnetizing inductance is equal to the predicted value in the previous chapter. Also the measured total resistant of the structure is $63m\Omega$ which is close to the achieved value in the optimized parameters and accordingly, there is no need to add extra resistor to the circuit.

AST 3003 ac source will provide the input voltage of the structure at the maximum possible frequency which is $4kHz$. Based on the equivalent circuit presented in Fig. 5.4, the capacitor values can be calculated as follows. First, using (4.6) and operating frequency, ω which is $2\pi \times 4000$, the value of C_1 in the resonance frequency of primary leakage inductance, L_{s_1} is obtained:

$$C_1 = \frac{1}{L_{s_1}\omega^2} = 30.86 \approx 30 \ \mu F \ . \tag{5.1}$$

The value of the secondary side capacitor, C_2 can be obtained using the lagging phase of the secondary current from the optimization and (4.7):

$$C_2 = \frac{1}{\omega \left(\omega L_{s_2} - R_L \tan\left(\theta_2\right)\right)} \tag{5.2}$$

Based on the measured value of $46.69\mu H$ for the secondary side leakage inductance , L_{s_2}, optimized values of θ_2 and R_L which are $-85.87°$ and 0.06Ω respectively and, (5.2), C_2 is:

$$C_2 = 19.84 \approx 20 \ \mu F \ . \tag{5.3}$$

Changing the value of C_2 to the standard value of $20\mu F$ will decrease the value of θ_2 from $-85.87°$ to $-85.79°$. Based on the calculated values, input voltage can be

calculated using (4.42):

$$V_{in} = \left(\frac{\omega M \sqrt{1 + \tan{(\theta_2)}^2}}{\sqrt{1 + \left(\tan{(\theta_2)} + \frac{\omega M}{R_L} \right)^2}} \right) |I_1| = 14.83 \ V \qquad (5.4)$$

Using the actual value of θ_2 and (4.9) the actual primary side lagging angle is:

$$\theta_1 = \left(\frac{\pi}{2} + \theta_2 - \arctan \left(\tan{(\theta_2)} + \frac{\omega M}{R_L} \right) \right) \times \frac{180}{\pi} = 86.19° \ . \qquad (5.5)$$

The last parameter is the secondary current value which can be obtained from (4.41):

$$I_2 = \frac{\omega M}{R_L \sqrt{1 + \left(\tan{(\theta_2)} + \frac{\omega M}{R_L} \right)^2}} |I_1| = 18.13 \ A \ . \qquad (5.6)$$

According to modified values and using (4.4), the magnitude of the magnetic flux density at $3cm$ from the lower coil and $5cm$ from the upper coil is $5.41mT$ which follows the FEM calculated value of $5.9mT$ from Ansys. In the next chapter the actual value of the magnetic field is obtained from the structure.

5.1.2   Experimental Verification

To obtain the required capacitors, two series connected 60 μF and two parallel connected 10 μF capacitors are used at the primary and secondary coils respectively. The F.W. Bell 5180 with transverse probe [45] is used to measure the ac magnetic flux density at various distances. To increase the measurement accuracy, a holder is designed for the Gauss meter probe.

The magnitude of flux density is measured for different distances in the proposed structure to verify the analytical approaches. According to $14.92V$ input voltage, the actual values of the primary and secondary current are $19.59A$ and $18.62A$ respectively with the phase difference of $172.5°$. As a reference point, both currents waveform and the measured magnetic flux density at $3cm$ from the lower coil is presented in Fig.5.5.
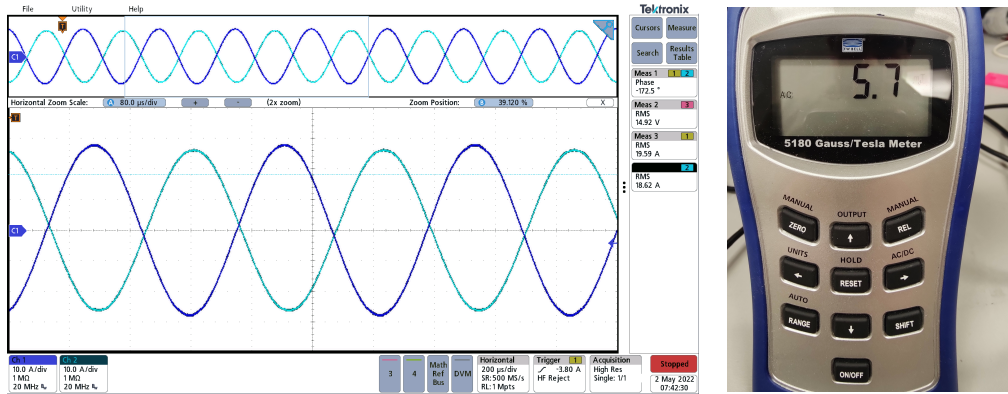
Figure 5.5: Experiment obtained parameters (a) Current waveforms (b) Magnetic field measurement

The measured value is verified the analytical and FEM results with less than 10% error:

Table 5.2: Flux Density and error

Method	$\mathbf{B}|_{3cm}$	error
Experiment	5.7 mT	0
Maxwell	6.27 mT	10%
Analytical	5.3 mT	7.01%

The magnetic flux density complete result curve for different methods is presented in Fig.5.6 which verify the accuracy of the analytical and FEM methods to predict the magnetic flux density between the coils.
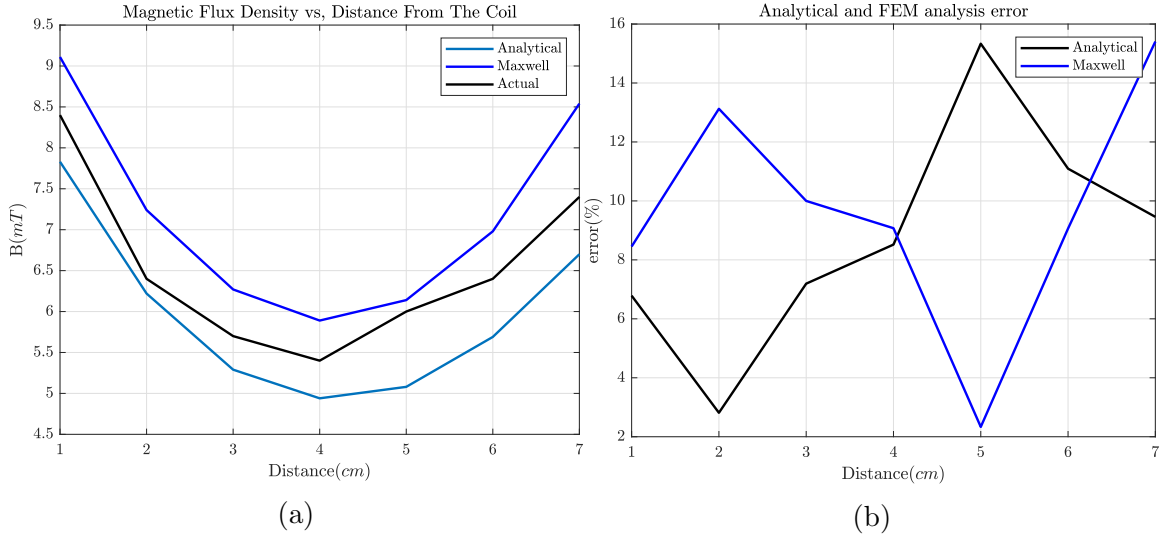
Figure 5.6: Different methods accuracy (a) Magnetic Field (b) Error

5.2 Summary

In this chapter the experimental setup is implemented to obtain the actual magnetic field from the proposed structure. The experimental results are compared with the analytical and FEM obtained results. It is shown that both FEM methods and analytical method can model the proposed structure precisely with less than 10% error in al distances between the coils.

Chapter 6

Conclusion and Future Works

In this work a novel structure is introduced for separating the non-ferrous metal scraps using the applied Lorentz force from the induced eddy current. The main contributions and conclusions of this dissertation is listed:

1. Theory of eddy current separators and different ways of separating non-ferrous metals is introduced including the conventional using of heavy noisy expensive magnetic drums and inefficient static separators.

2. Analytical model of a most simple structure consists of a simple coil without any core is derived using the Biot-Savart law. E ferrite core added to the structure to improve the magnetic field outside the core. Mirror method introduced to model the effect of core. Two cases considered for the non-planar structure to analyze the effect of core size on maintaining the magnetic field and it is shown that, the largest E core would have higher magnetic field compare to concentrated structure. Second coil added to improve the magnetic field in the desired distance.

3. Novel planar structure is proposed with partially covered core sticks and structural design variables. Air core planar structure analytical model is derived using the magnetic vector potential. Next, modified mirror method is introduced to model the effect of the core bars. Second coil added to improve the

magnetic field. The superiority of the planar structure over the non-planar is shown by performing detailed multi-dimensional comparison.

4. The optimization cost function to maximize the magnetic field of the proposed structure is derived. The optimized scaled down product optimization cost function is achieved and then solved which leads to optimized structure parameters. The scaled down prototype of the structure is implemented with industrial 3D printers.

5. The experiment setup is implemented and the magnetic field results are obtained. The experimental values verified both FEM and proposed analytical model of the structure.

6. In contrast with industrial sized separators, the prototype structure is 90% smaller and provides the magnetic flux density equal to 10% of the conventional magnetic drum separators with very low power consumption and zero air and noise pollution.

7. The proposed planar separator is light weight and has a simple and easy to assemble structure without any need for special and expensive materials.The power electronic based control unit of the proposed structure gives it flexibility to change the current and frequency based on the size of metal scraps spontaneously with almost zero startup time.

Table 6.1: Proposed and conventional method comparison

Type	$\mathbf{B}|_{3cm}$	Frequency	Input Power
Magnetic Drum	50 mT	50 Hz	11 kW
Prototype at 10%	5.7 mT	4000 Hz	0.3 kW

6.1 Future Work

There are some possibilities for the future work to improve the proposed novel approach for separating the non-ferrous metal particles. Some of the options for future work include:

1. Optimized industrial sized separator can be implemented to obtain the full potential of the proposed static eddy current separator in recycling non-ferrous metal scraps.

2. Controllable power converter can be designed to power the industrial separator at high frequencies for better separation of small metal particles and to avoid audible noise pollution in the segregation plants.

3. The optimization cost function can be redefined by including the power loss, and other symmetrical assumptions such as the number of turns in the primary and secondary winding to achieve better performance.

Bibliography

[1] G. of Canada, *Solid waste diversion and disposal*, https://www.canada.ca/en/ environment-climate-change/services/environmental-indicators/solid-waste-diversion-disposal.html, note = Accessed: 2022-02-01, 2022.

[2] G. of Canada, *Aluminum facts*, https://www.nrcan.gc.ca/our-natural-resources/minerals-mining/minerals-metals-facts/aluminum-facts/20510, Accessed: 2022-02-01, 2022.

[3] R. C. of British Columbia, *Waste prevention facts*, https://www.rcbc.ca/files/ u6/rg_100217_Waste_Prevention_Facts.pdf, Accessed: 2022-02-01, 2021.

[4] J. Oberteuffer, "Magnetic separation: A review of principles, devices, and applications," *IEEE Transactions on Magnetics*, vol. 10, no. 2, pp. 223–238, 1974.

[5] E. Thomas, *Ore separator*, US Patent 400,317, 1889.

[6] M. Hiram, *Magnetic separator*, US Patent 402,684, 1889.

[7] M. Richard, *Electro magnetic separator*, US Patent 411,899, 1889.

[8] Y. R. Smith, J. R. Nagel, and R. K. Rajamani, "Eddy current separation for recovery of non-ferrous metallic particles: A comprehensive review," *Minerals Engineering*, vol. 133, pp. 149–159, 2019.

[9] J. R. Nagel, "Induced eddy currents in simple conductive geometries: Mathematical formalism describes the excitation of electrical eddy currents in a time-varying magnetic field," *IEEE Antennas and Propagation Magazine*, vol. 60, no. 1, pp. 81–88, 2018. DOI: 10.1109/MAP.2017.2774206.

[10] P. R. Rony, "The electromagnetic levitation of metals," 1964.

[11] J. D. Ray, J. R. Nagel, D. Cohrs, and R. K. Rajamani, "Forces on particles in time-varying magnetic fields," *KONA Powder and Particle Journal*, vol. 35, pp. 251–257, 2018.

[12] M. J. Bartholemew, *Concentrator*, US Patent 1,417,189, 1922.

[13] W. H. Benson and T. H. Falconer, *Electrodynamic separator*, US Patent 3,448,857, 1969.

[14] H. J. van der Valk, W. L. Dalmijn, and W. Duyvesteyn, "Eddy-current separation methods with permanent magnets for the recovery of non-ferrous metals and alloys," *Erzmetall*, vol. 41, no. 5, pp. 266–274, 1988.

[15] J. Julius, *Apparatus for separating non-magnetizable metals from a solid mixture*, US Patent 5,057,210, 1991.

[16] E. H. Roos, *Method and apparatus for separating particulate material according to conductivity*, US Patent 5,161,695, 1992.

[17] M. Lungu and Z. Schlett, "Vertical drum eddy-current separator with permanent magnets," *International journal of mineral processing*, vol. 63, no. 4, pp. 207–216, 2001.

[18] Z Schlett and M Lungu, "Eddy-current separator with inclined magnetic disc," *Minerals engineering*, vol. 15, no. 5, pp. 365–367, 2002.

[19] M. Lungu, "Separation of small nonferrous particles using an angular rotary drum eddy-current separator with permanent magnets," *International Journal of Mineral Processing*, vol. 78, no. 1, pp. 22–30, 2005.

[20] W. Yao *et al.*, "Development of an eddy-current separation equipment with high gradient superconducting magnet," *IEEE Transactions on Applied Superconductivity*, vol. 25, no. 3, pp. 1–4, 2014.

[21] Goudsmith, *Eddyfines - eddy current separators features*, https://www.goudsmitmagnets.com/solutions/magnetic-recycling-sorting/eddy-current-separators/eddyfines.html?sku=E0139716, Accessed: 2022-02-05, 2016.

[22] L. Royal, *Ore concentration*, US Patent 1,829,565, 1931.

[23] E. Schlömann, "Separation of nonmagnetic metals from solid waste by permanent magnets. i. theory," *Journal of Applied Physics*, vol. 46, no. 11, pp. 5012–5021, 1975.

[24] E Schloemann and M Reiner, "Nonferrous metal separators for small particles," *IEEE Transactions on Magnetics*, vol. 15, no. 6, pp. 1535–1537, 1979.

[25] M. S. Zakharova *et al.*, *Method of and apparatus for electrodynamic separation of nonmagnetic free-flowing materials*, US Patent 4,238,323, 1980.

[26] R. G. Arnold and D. M. Bills, *Material separator apparatus*, US Patent 5,423,433, 1995.

[27] J. R. Nagel, D. Cohrs, J. Salgado, and R. K. Rajamani, "Electrodynamic sorting of industrial scrap metal," *KONA Powder and Particle Journal*, p. 2 020 015, 2020.

[28] I. T. U. (ITU), *Wireless power transmission using technologies other than radio frequency beam*, https://www.itu.int/dms_pub/itu-r/opb/rep/R-REP-SM.2303-2-2017-PDF-E.pdf, Accessed: 2022-06-15, 2017.

[29] C. R. Paul, *Inductance: loop and partial*. John Wiley & Sons, 2011.

[30] P Hammond, "Electric and magnetic images," *Proceedings of the IEE-Part C: Monographs*, vol. 107, no. 12, pp. 306–313, 1960.

[31] Ferroxcube, *E30/15/7 specifications*, https://www.ferroxcube.com/upload/media/product/file/Pr_ds/E30_15_7.pdf, Accessed: 2021-10-05, 2016.

[32] Ferroxcube, *3c94 material specifications*, https://www.ferroxcube.com/upload/media/product/file/MDS/3c94.pdf, Accessed: 2021-10-07, 2008.

[33] S. Mukherjee, Y. Gao, and D. Maksimović, "Reduction of ac winding losses due to fringing-field effects in high-frequency inductors with orthogonal air gaps," *IEEE Transactions on Power Electronics*, vol. 36, no. 1, pp. 815–828, 2020.

[34] R. Schlesinger and J. Biela, "Comparison of analytical models of transformer leakage inductance: Accuracy versus computational effort," *IEEE Transactions on Power Electronics*, vol. 36, no. 1, pp. 146–156, 2020.

[35] A. Zisserman, R. Saunders, and J. Caldwell, "Analytic solutions for axisymmetric magnetostatic systems involving iron," *IEEE Transactions on Magnetics*, vol. 23, no. 6, pp. 3895–3902, 1987. DOI: 10.1109/TMAG.1987.1065773.

[36] X. Margueron, A. Besri, P.-O. Jeannin, J.-P. Keradec, and G. Parent, "Complete analytical calculation of static leakage parameters: A step toward hf transformer optimization," *IEEE Transactions on Industry Applications*, vol. 46, no. 3, pp. 1055–1063, 2010.

[37] M. Lambert, F. Sirois, M. Martinez-Duro, and J. Mahseredjian, "Analytical calculation of leakage inductance for low-frequency transformer modeling," *IEEE Transactions on Power Delivery*, vol. 28, no. 1, pp. 507–515, 2013. DOI: 10.1109/TPWRD.2012.2225451.

[38] Ferroxcube, *E80/38/20 specifications*, https://www.ferroxcube.com/upload/media/product/file/Pr_ds/E80_38_20.pdf, Accessed: 2021-10-05, 2016.

[39] J. D. Ray, J. R. Nagel, D. Cohrs, and R. K. Rajamani, "Forces on particles in time-varying magnetic fields," *KONA Powder and Particle Journal*, vol. 35, pp. 251–257, 2018. DOI: 10.14356/kona.2018016.

[40] Strasys, *Fortus 450mc printer brochure*, https://www.stratasys.com/siteassets/3d-printers/printer-catalog/fdm-printers/fortus-450mc/br_fdm_fortus450mc_0721a.pdf?v=48edee, Accessed: 2022-02-05, 2015.

[41] Ferroxcube, *I 100/25/25 specifications*, https://www.ferroxcube.com/upload/media/product/file/Pr_ds/U100_57_25_I100_25_25.pdf, Accessed: 2021-10-05, 2016.

[42] AMETEK, *Ast3003 datasheet*, https://www.programmablepower.com/products/ac-power-sources/cf0377d8-96ed-4130-a0ad-641b16483a2a, Accessed: 2021-10-05, 2021.

[43] U. of Alberta, *Elko engineering garage*, https://confluence.garage.ualberta.ca/, Accessed: 2021-08-05, 2021.

[44] Strasys, *Asa material datasheet*, https://www.stratasys.com/siteassets/materials/materials-catalog/fdm-materials/asa/mds_fdm_asa_0921a.pdf?v=48e29d, Accessed: 2022-02-05, 2015.

[45] Bell, *Fw bell 5180 user manual*, https://fwbell.com/wp-content/uploads/2017/12/UN1260.pdf, Accessed: 2021-09-15, 2021.